TRIP Assisted Press Hardened Steel by the Anisothermal Bainitic Ferrite Transformation

T. Taylor[a]*, K. Kim[a], J. Zhang[a], D. Penney[b], J. Yanagimoto[a]

[a]The University of Tokyo, Department of Mechanical Engineering, 7-3-1 Hongo, Bunkyo-ku, Tokyo 113-8656, Japan (*tom.taylor@cem.t.u-tokyo.ac.jp, +81-3-5841-4885 (ex. 24885))

[b]Swansea University, Materials Research Centre, Swansea, SA1 8EN, United Kingdom

Abstract

A new steel chemical composition is combined with a new press hardening process, in which die-quenching is interrupted by opening the forming tool to permit slow cooling of the hot formed part through the anisothermal bainitic ferrite transformation. This promotes carbon partitioning to austenite before the forming tool is re-closed and die-quenching is resumed to near-ambient temperature. The final microstructure is predominantly bainitic ferrite with dispersions of martensite and up to 11 % retained austenite. Retained austenite can undergo stress induced transformation to martensite in an automobile crash event. The steel exhibits up to 25 % elongation and 930 MPa tensile strength. In contrast to traditional cold formable Transformation Induced Plasticity assisted steels, where retained austenite is consumed during work hardening of cold forming, here, the desired microstructure is achieved after hot forming meaning the retained austenite is more uniformly distributed within the formed part, which enhances energy absorption. The new steel chemical composition is carefully designed to provide optimal microstructural evolution within the constraints of the new press hardening process, yet relatively lean and manufacturer friendly. The new press hardening process is energy efficient as secondary heating is not required since retarded cooling through the bainitic ferrite transformation is provided by residual heat accumulation of the newly developed titanium alloy forming tool. Development of the new technology is demonstrated by press hardening experiments, tensile testing, microstructural

analysis, transversal & axial crush testing of formed parts and numerical simulation of crush testing, including a new modelling technique that more accurately simulates deformation of hot versus cold formed parts. Results show a 22 % increase to energy absorption under axial crushing compared to traditional cold formed Transformation Induced Plasticity assisted steels owing to greater work hardening capacity in formed radii of the part, which are shown to be exposed to the highest stresses during crushing.

Key words: retained austenite; stress induced transformation; Electron Back Scattered Diffraction; hot stamping; crush testing; numerical simulation

Introduction

(Zackay et al., 1967) first reported the Transformation Induced Plasticity (TRIP)' effect in 1967 during investigation of austenitic stainless steels. The authors discovered unusually high uniform elongation values, which they attributed to stress or strain induced transformation of austenite to martensite, giving rise to dilatation and internal plastic strain, hence the term TRIP. Mild carbon low alloy TRIP steels, exploiting the same phenomenon discovered by (Zackey et al, 1967) were developed by the steel industry in the early 1990s and continue to gain much attention within academic research owing to the impressive combinations of strength and ductility. (Tan et al., 2020) applied different hot rolling, quenching and partitioning sequences to a controlled steel chemical composition to obtain eight different TRIP steel products with different microstructures and then evaluated the effect on mechanical properties. Compared to Dual Phase (DP) steels characterised by microstructures of ferrite and martensite, exhibiting an ultimate tensile strength-total elongation product of approximately 15 GPa.%, TRIP steels exhibit much higher values of up to 25 GPa.%. The characteristically impressive strength-ductility combination of TRIP steels provides superior cold formability and potentially, superior application performance, such as automobile crash performance. (Oliver et al., 2006) conducted impact crash box testing on DP and TRIP steels with equivalent tensile strength. For a given strength category, the TRIP steels

with enhanced ductility consistently exhibited superior energy absorption by preventing folded regions of the deformed crash box from splitting.

(Sakuma et al., 1995) documented development of first generation TRIP steels by the steel industry in the early 1990s. Chemical compositions are typically of 0.15-0.25%C, 1-2%Mn and 1.5%Si and are processed during hot rolling or strip annealing to exhibit a multi-phase microstructure of predominantly (proeutectoid) ferrite, with dispersions of bainitic ferrite, martensite and 10-15% retained austenite. The silicon content retards iron carbide precipitation during bainite formation giving rise to carbide-free bainitic ferrite with excess carbon over and above the ferrite saturation limit partitioning to austenite and remaining in solid solution. The carbon enriched austenite is then stabilised at ambient temperature. The retained austenite is designed to be stress induced transformed to martensite during plastic deformation, as originally cited by (Zackay et al., 1967), but in this manner, can be achieved with the inexpensive addition of just 1.5%Si rather than 20%(Cr+Ni) in austenitic stainless steel. While TRIP steels inherit their name from the transformation induced plasticity effect originally cited by (Zackay et al., 1967), (Bhadeshia, 2002) has mathematically demonstrated that only 2 % of the uniform elongation value may be attributed to the TRIP effect, with for the most part, the impressive strength-ductility combination attributed to ‘composite deformation’ behaviour, where ductility of ferrite is exploited early during deformation

and then hardness of martensite resulting from stress induced transformation exploited late during deformation.

While economical, the typical silicon content of up to 1.5% has significantly restricted application of first generation TRIP steels. Slab cracking, high rolling loads, poor weldability and poor metallic coatability are the major drawbacks. To overcome these problems, second generation TRIP steels (sometimes called TRIP assisted DP steels) with silicon content partially substituted by aluminium have been developed. (Mein et al., 2012) investigated a commercial C-Mn-Cr DP steel and an equivalent experimental steel with the addition of 0.52%Al. The aluminium addition not only allows for higher percentages of retained austenite, but also broadens the processing window of DP steels by raising the A3 temperature to reduce distribution of mechanical properties.

The next problem identified with first and second generation TRIP steels has been relatively low proof to ultimate tensile strength ratio, typically of the order of 0.5, compared to 0.6 of DP steels and 0.8 of martensitic steels. While the low proof to ultimate ratio is indicative of high work hardenability and energy absorption, many automotive structural parts require a minimum proof strength. Therefore, parts may require over forming (work hardening) in order to meet the minimum requirement. To overcome this, third generation TRIP assisted Bainitic Ferrite (TBF) steels have been developed. (Bachmaier et al., 2013) illustrated the design principles behind TBF

steels, consisting predominantly of bainitic ferrite with retained austenite dispersions produced by isothermal holding in the bainitic phase field following rapid cooling from the austenite phase conducted either on the Run Out Table following hot rolling, or during the continuous annealing cycle following cold rolling.

(Ridderstrale, 1977) developed the original Press Hardened Steel (PHS) technology to overcome poor formability and high springback of ultrahigh strength martensitic steels. The steel blank (typical chemical composition of 0.20-0.25%C, 1.2%Mn and 30-50ppmB) is furnace heated to the austenite phase, transferred to the water cooled forming tool, formed in the austenite phase and then die-quenched to martensite, giving rise to tensile strength and total elongation values of 1400-1600 MPa and 3-6 % respectively. The automotive industry desires lightweighting (primarily to reduce exhaust emissions and fuel consumption). Down-gauging reduces weight, but compromises formability and springback. These compromises are more significant when strength is increased, but they still exist for lower strength steels. Press hardening offers exceptional formability and almost eliminates springback, thus press hardening has gained attention for lower strength parts. (Naderi et al., 2011) developed three C-Mn-Cr steels with chemical compositions of 0.14-0.19%C, 1.45-1.71%Mn and 0.01-0.55%Cr. Following press hardening, the three steels gave rise to multiphase microstructures of ferrite, bainite and martensite exhibiting tensile strength of up to 910 MPa and total elongation of up to 9.3 %.

The design principles behind TBF steels are compatible with the press hardening process, consisting of rapid cooling from the austenite phase to bainite and / or martensite. However, in order to achieve the isothermal holding step in the bainitic phase field following rapid cooling from austenite, the original press hardening process requires modification. (Liu et al., 2011) made an attempt towards this by interrupting die-quenching in the temperature range of 280-320 ^{o}C with a secondary isothermal heating step for up to 60 s before die-quenching is resumed to near-ambient temperature. Using a steel with chemical composition of 0.22%C, 1.58%Mn and 0.81%Si, the result was reported to be inter-lath retained austenite within the martensitic matrix, giving rise to a retained austenite volume fraction of 18 %, ultimate tensile strength of 1510 MPa and total elongation of 15 %. While the result is impressive, modification to the press hardening line with the secondary heating step is costly in terms of both infrastructure requirements and energy consumption. (Xu et al., 2020) introduced a similar idea as above, but instead used a first generation TRIP steel of 0.2%C, 1.9%Mn and 1.4%Si; and instead of isothermal holding, used retarded cooling by pre-heating the forming tool to 200 ^{o}C and opening the forming tool in the region of 300-200 ^{o}C for up to 60 s to conduct the anisothermal bainitic ferrite transformation. The optimum result was a retained austenite volume fraction of 11 %, tensile strength of 1449 MPa and total elongation of 14.5 %. These impressive results, which represent properties of the formed part are very similar to the traditional cold formable strip TRIP and TBF steels. However, the

retained austenite in the latter is consumed during the plastic strain of forming. (Oliver et al., 2007) conducted pre-strain tensile tests on a commercial TRIP steel, showing that pre-strain of 10 % reduced the retained austenite volume fraction from 10 to 5 %. Proof strength was raised from 550 to 825 MPa owing to work hardening, while total elongation was reduced from 30 to 15 % owing to degradation of the stress induced transformation effect. Thus, to compare like for like, the measured mechanical properties of a traditional cold formed TRIP or TBF steel part (in formed regions) will be inferior to the mechanical properties of the part produced by (Xu et al., 2020), since in the latter the optimal retained austenite volume fraction and stress induced transformation capability is determined after forming and thus, uniformly distributed throughout the part. However, as previously mentioned, the first generation TRIP steel used by (Xu et al., 2020), rich in silicon, is unfavourable because of manufacturing drawbacks and thus, the technology is unlikely to reach commercialisation. Pre-heating the forming tool also necessitates modification to the press hardening line, which increases the infrastructure requirements and energy consumption and reduces the production efficiency. In addition, pre-heating the forming tool decreases the die-quenching rate, limiting capability of the process to produce a variety of microstructures (particularly with limited ferrite volume fractions) across parts with different dimensions and gauges.

In this paper, we introduce a new steel chemical composition combined with a new press hardening process in which die-quenching is interrupted by opening the forming tool at a temperature in the bainitic phase field. The resulting slow cooling of the hot formed part through the anisothermal bainitic ferrite transformation allows carbon partitioning to austenite to occur. The forming tool is then re-closed and die-quenching is resumed to near-ambient temperature. The new steel chemical composition is carefully designed to provide optimal microstructural evolution within the constraints of the new press hardening process, yet relatively lean, manufacturer friendly and compatible with conventional steelmaking, strip rolling, metallic coating and welding practices. The new press hardening process is economical and energy efficient as secondary heating is not required, since retarded cooling through the bainitic ferrite transformation is provided by residual heat accumulation of the newly developed titanium alloy forming tool following hot forming. Fig. 1 illustrates the principal advantage of the proposed TRIP assisted PHS technology compared to traditional cold formable TRIP (and TBF) steels.

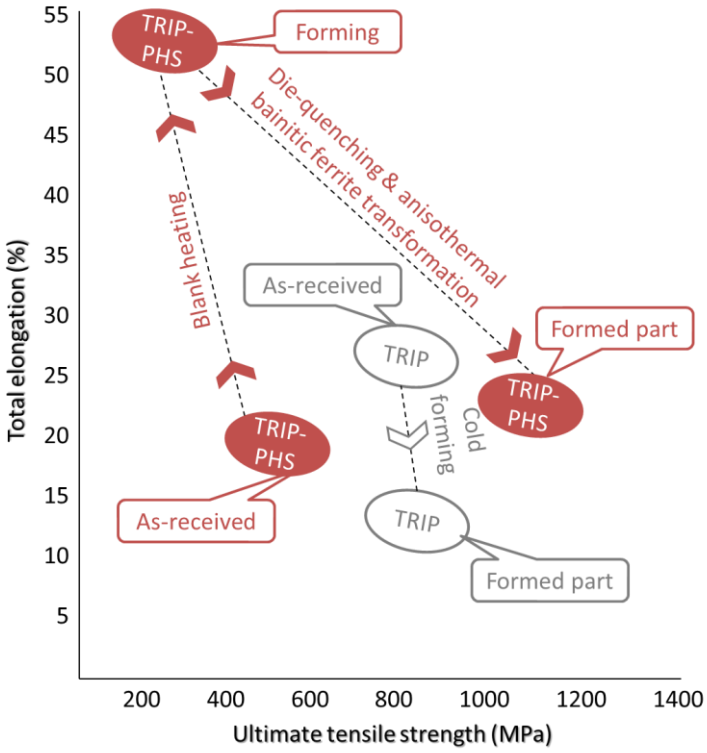

Fig. 1: Schematic illustration of the improved formability and formed part mechanical properties of the proposed TRIP assisted PHS technology compared to traditional cold formable TRIP steels

Experimental

New Press Hardening Process

The new press hardening process is schematically illustrated by Fig. 2a. The steel blank is furnace heated above the A3 temperature, transferred to the water cooled forming tool and hot formed into the part geometry while in the highly formable and isotropic austenite phase, as per the original press hardening process by (Ridderstrale, 1977). Die-quenching from austenite is interrupted by opening the forming tool at a temperature in the bainitic phase field between the A1

and Ms temperatures, in a similar fashion as per the processes by (Liu et al., 2011) and (Xu et al., 2020). However, in this new process, there is no secondary heating step, neither by isothermal heating as by (Liu et al., 2011), nor by pre-heating the forming tool to retard cooling as by (Xu et al., 2020). Instead, the hot formed part is slowly cooled through the anisothermal bainitic ferrite transformation, with cooling retarded by residual heat of the forming tool following hot forming. Fig. 2b clearly illustrates the novelty of the new process compared to the previous processes. The forming tool is composed of an alloy with relatively low thermal conductivity, such as titanium alloy, as developed by (Taylor et al., in-press); and water cooling of the forming tool is disabled during interrupted die-quenching to maximise retardation of cooling. Subsequently, the forming tool is re-closed, water cooling of the forming tool is re-activated and die-quenching is resumed to near-ambient temperature. By employing different parameters, including furnace soaking temperature prior to hot forming and die-quenching; and tool-open temperature-time during interrupted die-quenching, a wide range of microstructures and mechanical properties are theoretically achievable from a given steel chemical composition. However, the principal microstructure targeted is predominantly of bainitic ferrite with dispersions of martensite and retained austenite. Retained austenite is designed to undergo stress induced transformation to martensite during application of the formed part such as an automobile crash event, giving rise to the characteristically impressive strength-ductility combination of TRIP assisted steels.

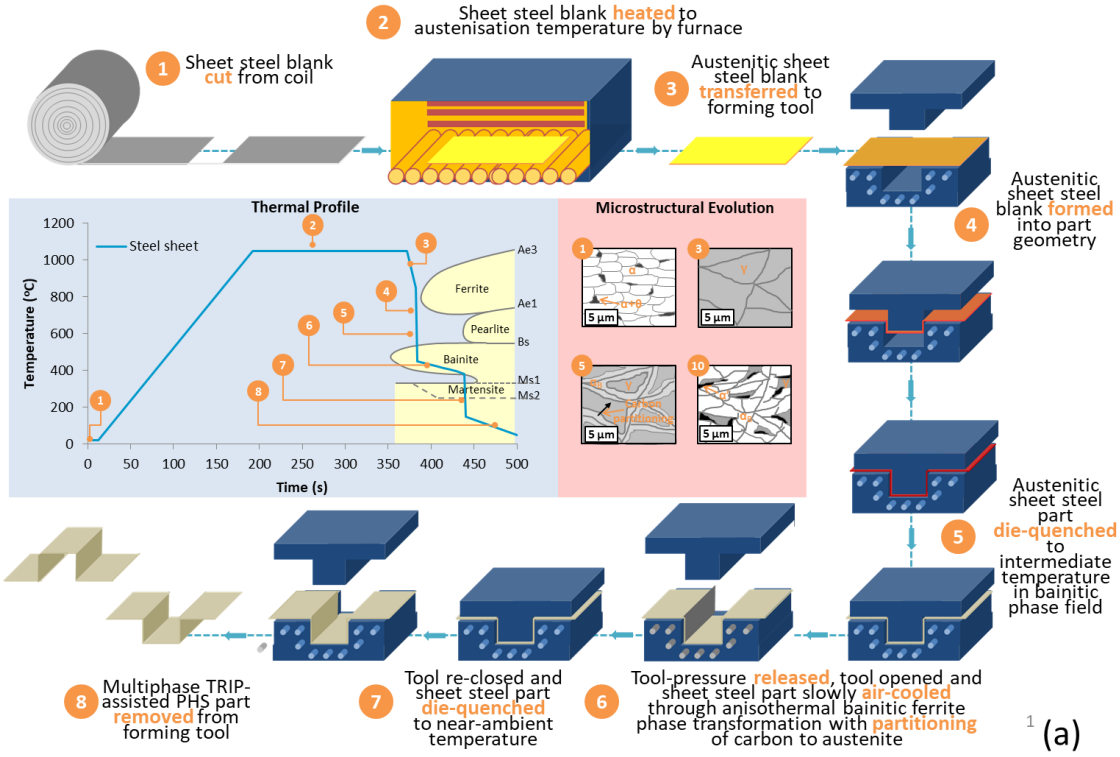
2 Sheet steel blank heated to austenisation temperature by furnace
1 Sheet steel blank cut from coil
3 Austenitic sheet steel blank transferred to forming tool
4 Austenitic sheet steel blank formed into part geometry
5 Austenitic sheet steel part die-quenched to intermediate temperature in bainitic phase field
6 Tool-pressure released, tool opened and sheet steel part slowly air-cooled through anisothermal bainitic ferrite phase transformation with partitioning of carbon to austenite
7 Tool re-closed and sheet steel part die-quenched to near-ambient temperature
8 Multiphase TRIP-assisted PHS part removed from forming tool
Thermal Profile
Steel sheet
Temperature (°C)
Time (s)
Ae3
Ae1
Bs
Ms1
Ms2
Ferrite
Pearlite
Bainite
Martensite
Microstructural Evolution
5 µm
(a)

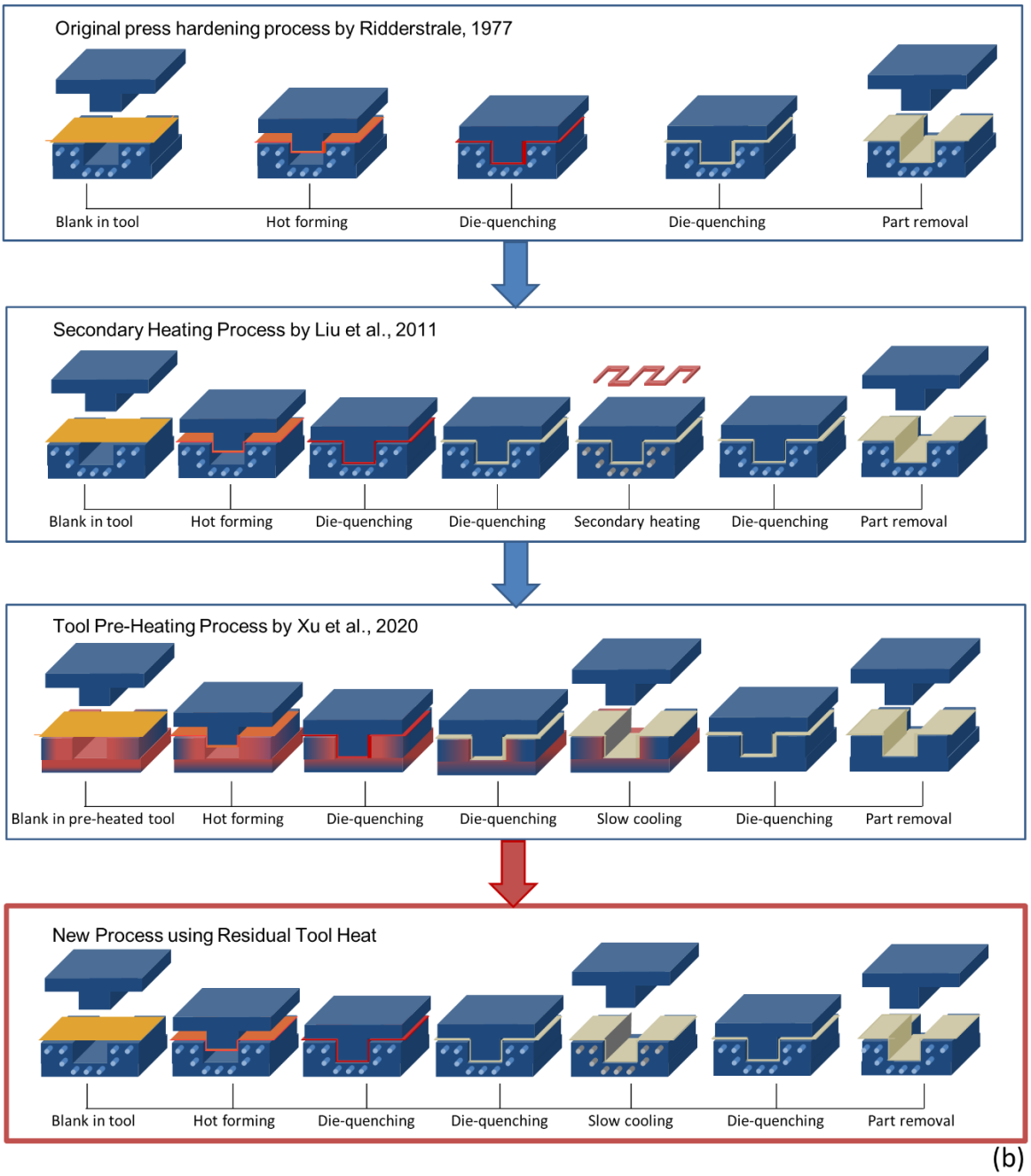

Fig. 2: Schematic illustration of (a) the new press hardening process and (b) novelty from previous processes

New Press Hardened Steel Chemical Composition

To achieve optimal microstructural evolution within the constraints of the new press hardening process, a new steel chemical composition is required which can achieve austenisation with soaking temperature ideally less than 1000 ^{o}C, avoid proeutectoid ferrite formation and achieve sufficient partitioning of carbon to austenite with the limited temperature and time available without secondary heating. The chemical composition of the new steel denoted as 20MnSiAlPB5 is shown in Table 1. The design principles are based on the well-known effects of alloying elements on steel, such as those documented by (Bain, 1939). Carbon content is selected to provide interstitial solid solution strengthening, quench hardenability, low A3 temperature and stabilisation of austenite at ambient temperature following partitioning from bainitic ferrite, where at least 0.1%C, or ideally at least 0.15%C is required for the latter, while maintaining sufficiently low carbon equivalent for conventional resistance spot-welding techniques. Manganese content is selected to provide substitutional solid solution strengthening, quench hardenability and stabilisation of austenite at ambient temperature. It also minimises segregation during conventional steelmaking and casting practices (where segregation typically becomes significant with more than 1.5%Mn) and maintains sufficiently low carbon equivalent. Silicon, aluminium and phosphorus prevent carbide precipitation in carbon enriched austenite during bainitic ferrite formation, thus enabling the Ms temperature of the remaining untransformed austenite to be depressed below ambient

temperature. Silicon, aluminium and phosphorus contents are selected to provide the optimal balance of carbide precipitation retardation, kinetics of the anisothermal bainitic ferrite transformation, weldability, coatability and manufacturability. Silicon content is selected as the dominant carbide precipitation retardant, but is limited to minimise formation of surface-bound silicates that impede hot rolling, cold rolling and coating of strip steels when at levels greater than 0.7%. Aluminium is limited to preserve weldability and minimise nozzle blockage during steelmaking and casting. Aluminium increases kinetics of the anisothermal bainitic ferrite transformation so that appreciable volume fractions of austenite can be retained at ambient temperature during the limited time available during the new press hardening process. Phosphorus is present to limit silicon and aluminium contents and to providing satisfactory carbide precipitation retardation. Phosphorus is limited to around 0.08% to maintain acceptable weldability. Niobium is added to form niobium carbide precipitates and in turn to provide austenitic grain size refinement that increases the kinetics of the anisothermal bainitic ferrite transformation. Niobium is limited to no more than 0.04% due to the problems it introduces during strip annealing by narrowing the recrystallisation to austenisation process window. Titanium is added to form titanium nitride precipitates and in turn to enable boron to remain un-bonded in solid solution. Titanium content of 0.03% reflects the titanium to nitrogen stoichiometric ratio of 3.14:1. Boron is added for hardenability so to avoid proeutectoid ferrite formation. Thus, the targeted

microstructure is predominantly bainitic ferrite with dispersions of martensite and retained austenite. The 20MnSiAlPB5 steel was cast, hot rolled and cold rolled to 1.0 mm gauge strip in the laboratory, with the as-received material representing hard-iron (non-annealed) material. Two commercial steels, denoted 10MnSi15 and 20MnSi15, used for producing commercial first generation TRIP steels with minimum ultimate tensile strengths of 580 and 780 MPa respectively, were included for benchmarking (Table 1). The as-received commercial materials represented cold rolled annealed products with 1.0 mm gauge. The two commercial steels are designed for cold forming, prior to which, their microstructures are tailored during carefully controlled heat treatment on a continuous annealing line to form retained austenite needed for stress induced transformation capability. It is logical to test our new press hardening process with these existing commercial MnSi steels that are capable of retaining austenite (when subjected to a suitable heat treatment). The next step is then to develop a new steel chemical composition which is bespoke to the new process to yield a superior result. Furthermore, the new steel chemical composition is leaner and therefore more manufacturer friendly than the commercial steels.

Table 1: New press hardened steel 20MnSiAlPB5 and benchmark commercial steels 10MnSi15 & 20MnSi15 (values with units of wt% with Fe balance)

	C	Mn	Si	Al	P	Cr	Ti	Nb	N	B

20MnSiAlPB5	0.210	1.430	0.504	0.461	0.042	0.000	0.037	0.032	0.003	0.005
10MnSi15	0.083	1.460	1.350	0.139	0.009	0.025	0.015	0.001	0.004	0.000
20MnSi15	0.186	1.330	1.670	0.131	0.008	0.026	0.014	0.001	0.004	0.000

Press Hardening with Flat Dies for Tensile Testing and Optimisation of Process Parameters

Press hardening was conducted with a 50 kN thermo-mechanical testing machine equipped with induction heating and PID controller, as shown by Fig. 3a. Blanks with geometry of 30×15×1 mm suitable for subsequent tensile testing were press hardened between flat dies. The lower die exhibited a small notch (2 mm in length) to allow for access of the thermocouple welded to the blank, as shown by Fig. 3b. Three coupons for tensile testing and a sample for microstructural examination by high resolution Field Emission Gun Scanning Electron Microscopy (FEG-SEM) with Electron Back Scattered Diffraction (EBSD) and X-Ray Diffraction (XRD) were machined by Electrical Discharge Machining (EDM) from each press hardened blank, as shown by Fig. 3c. The tensile coupon design, illustrated by Fig. 3d, with gauge length of 5 mm was bespoke to meet the constraints of the experiment. All other parameters of tensile testing conformed to ISO 6892-

1:2016. Extension and thus strain was measured by Digital Image Correlation. Throughout, samples were tested in triplicate with mean results presented. Fig. 4 illustrates the Continuous Cooling Transformation (CCT) diagram for 20MnSiAlPB5 predicted by numerical simulation using JMatPro commercial software which was used to establish the test-matrix of experimental parameters for press hardening, including soaking temperatures and tool-open temperatures-times as critical variables, as highlighted in Fig. 5a. Heating rate was to be broken into two segments of 10 and 5 ^{o}C/s to replicate convective heating rates on industrial press hardening lines. However, the additional segment of 1 ^{o}C/s between 750 and 800 ^{o}C was necessary due to limited heating rate by induction through the ferrite to austenite transformation. The minimum soaking temperature was selected as 950 ^{o}C in light of the predicted A3 temperature of approximately 890 ^{o}C. Incrementally higher soaking temperatures of 1050 and 1150 ^{o}C, whilst unfavourable for higher energy consumption on industrial press hardening lines, were investigated for the purpose of greater austenitic grain growth and hardenability to retard proeutectoid ferrite formation. Soaking time was set at 30 s to ensure complete austenisation while preserving the testing machine. Transfer cooling rate of 15 ^{o}C/s and transfer cooling time of 10 s were selected to simulate natural air cooling of the blank during transfer from furnace to forming tool on industrial press hardening lines. Die-quenching rate of at least 100 ^{o}C/s was achieved by applying the 50 kN load (Fig. 5b) while simultaneously water cooling the dies to simulate conditions on industrial

press hardening lines and meet the predicted (by JMatPro software) critical cooling rate of 100 ^{o}C/s. Dies were fabricated from Ti-6Al-4V titanium alloy, marked by a relatively low thermal conductivity of 7 W/m.K to minimise heat loss during the anisothermal bainitic ferrite transformation. Tool-open temperatures of 350, 450 and 550 ^{o}C were selected to provide a range of temperatures in the bainitic phase field given predicted (by JMatPro software) Bs and Ms temperatures of approximately 580 and 400 ^{o}C respectively. Tool-open times of 60, 180 and 300 s were selected to investigate the optimal time for the anisothermal bainitic ferrite transformation. The PID controller allowed for heating and die-motion to be completely automated.

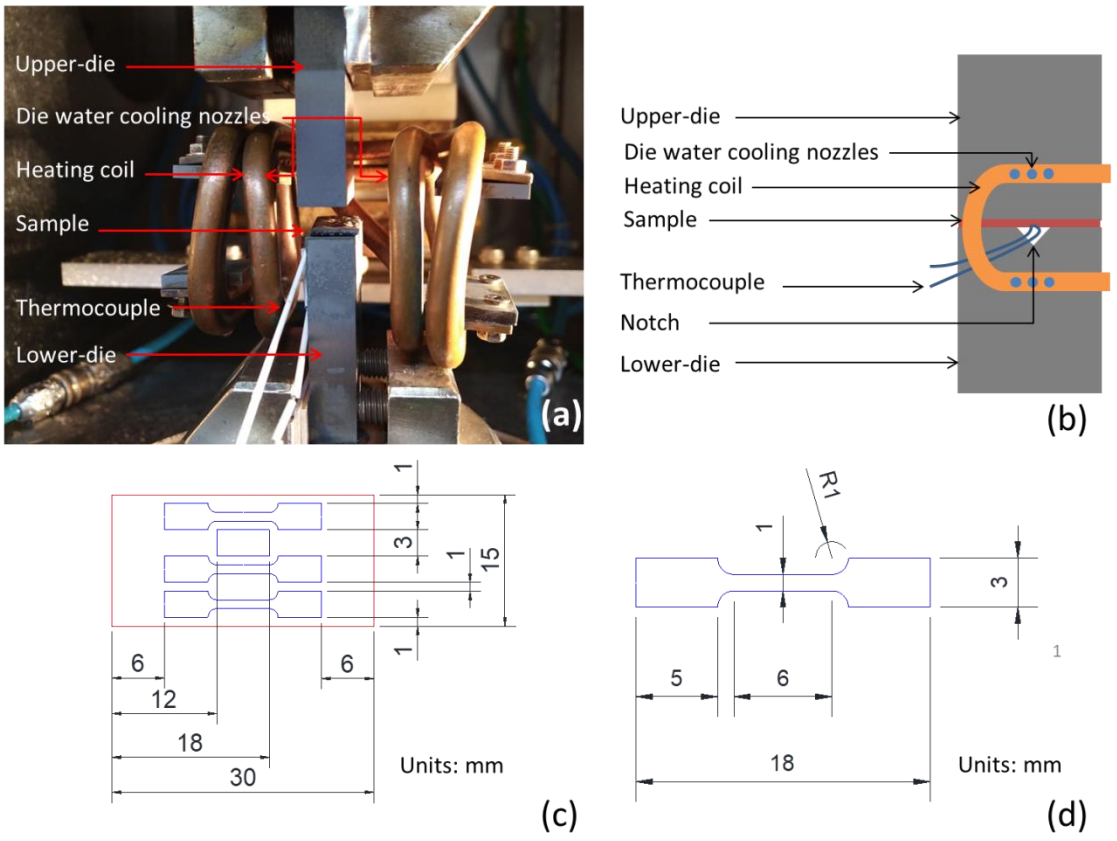

Fig. 3: Experimental set-up (a) 50 kN thermo-mechanical testing machine equipped with induction heating (b) schematic illustrating notch in lower die for access of thermocouple (c) configuration of tensile coupons and microstructural sample from press hardened blank (d) tensile coupon design

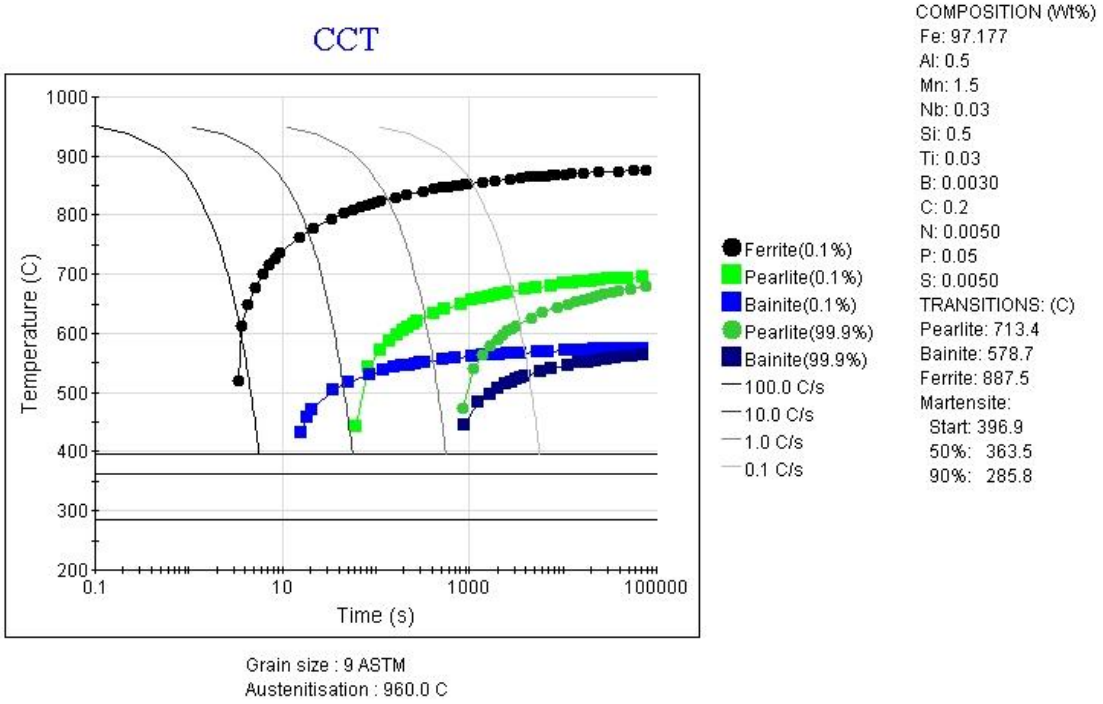

Fig. 4: 20MnSiAlPB5 CCT diagram predicted by numerical simulation

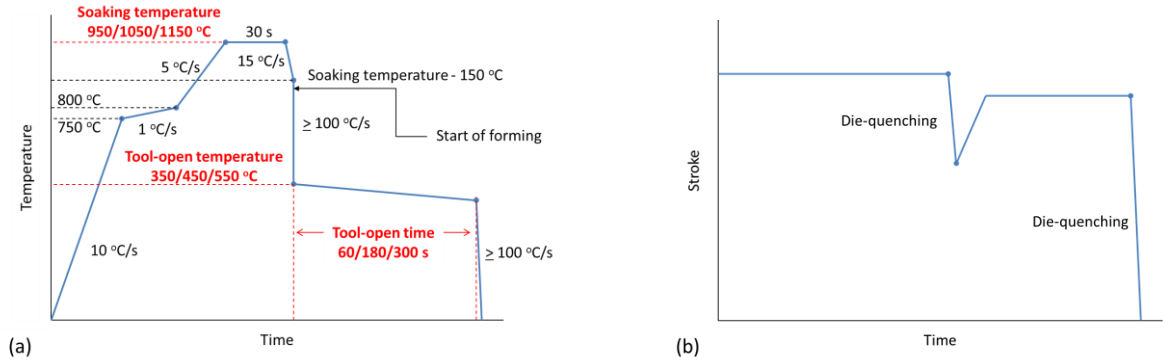

Fig. 5: Press hardening cycle illustrating (a) thermal parameters investigated and (b) application of stroke to control die-quenching

Characterisation of Microstructure and the Stress Induced Transformation

Dilatometry was conducted on 12×8 mm cylindrical billets to characterise microstructural evolution under the established optimal press hardening parameters. These findings were correlated to EBSD and XRD results to gain understanding of the optimally press hardened microstructure. For EBSD, including texture analysis and phase volume fraction measurement, five images were taken for a given specimen with mean results presented. Owing to the limited surface area that can practically be analysed by EBSD, XRD was used to confirm the austenite volume fraction over a larger surface area of 1 mm^2. Tensile strain was then applied to optimally press hardened specimens (using the tensile coupon design of Fig. 3d) to engineering strain values of 5, 10 and 15 % (without fracture), followed by EBSD and XRD examination of the strained gauge lengths to characterise microstructural evolution under replicated deformation (e.g. an automobile crash event) of a formed part. Analyses were conducted normal to the upper-surface.

Press Hardening for Transversal and Axial Crush Testing of Formed Parts

With the optimal press hardening parameters by the same thermo-mechanical testing machine established, Ti-6Al-4V titanium alloy dies were used to form the U-bend open box part geometry of Fig. 6a. To provide closer replication of an industrial press hardening line and to overcome the difficulty of induction heating a blank with relatively large aspect ratio, heating of blanks (50×50×1 mm) to the optimal soaking temperature was conducted with a box furnace, before transfer of blanks from furnace to forming tool in approximately 10 s and hot forming & die-quenching to the optimal tool-open parameters under the 50 kN load while simultaneously water cooling the dies. For evaluation of the effect of cold forming on the stress induced transformation of a TRIP assisted steel, 50×50×1 mm blanks of 20MnSiAlPB5 were also press hardened between flat dies to the optimal press hardening parameters and then cold formed. The hot and cold formed U-bend open box parts were used for evaluation of microstructure by EBSD, with characterisation conducted at the base, radius and side-wall of the part cross-section centreline, as schematically illustrated by Fig. 6b. Vickers hardness measurements with 10 kg load were conducted at 0.5 mm intervals along the cross-section centreline. This was conducted on three specimens with mean results presented. Additionally, the formed U-bend open box parts were subjected to transversal and axial crush testing under displacement rate of 1 mm/s, as shown by Fig. 6c and Fig. 6d respectively. For transversal crush testing, the former had radius of 3 mm, the

span was 30 mm and maximum displacement was 10 mm. For axial crush testing, maximum displacement was 30 mm. Transversal and axial crush testing were conducted on five specimens with mean results presented. Transversal crush testing is used for evaluation of deformation and deflection resistance, of utmost importance to parts of the automobile safety cell for maintenance of a survival space during a crash event. Axial crush testing is used for evaluation of energy absorption, of utmost importance to parts of the automobile crumple zones for smooth, predictable and controllable dissipation of impact energy during a crash event.

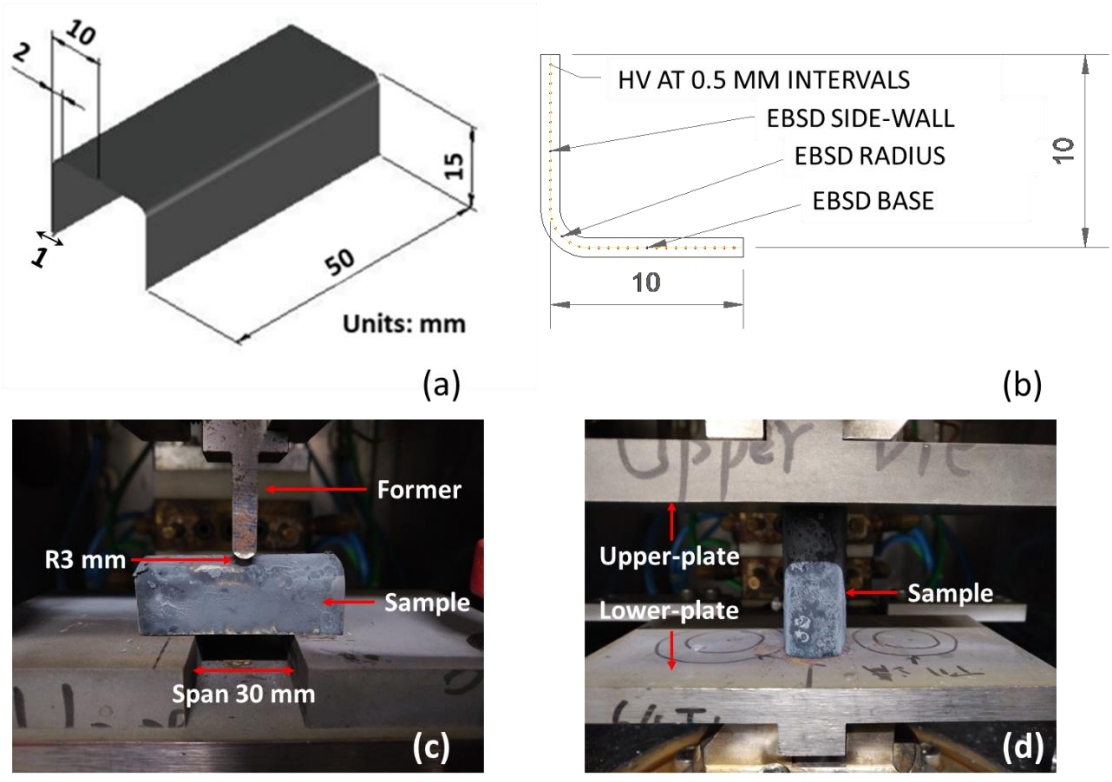

Fig. 6: Press hardening of U-bend open box part (a) part geometry (b) locations of characterisation points by EBSD and Vickers hardness testing (c) transversal crush testing (d) axial crush testing

Numerical Simulation of Transversal and Axial Crush Testing

When numerically simulating formed part performance testing, such as axial crush testing, it is common practice to apply the same material stress-strain data to the entirety of the part. For example, (Peixinho et al., 2003) conducted experimental and numerical simulation of axial crush testing on cold formed DP and TRIP steels. For each material, the authors applied the same stress-strain data throughout the part during numerical simulation. However, this approach can lead to inaccuracies in simulation, since during cold forming, work hardening takes place in the formed regions, giving rise to different material properties in different regions of the part. This is particularly true for TRIP assisted steels owing to their characteristically high work hardening rates and work hardening capacities. Consequently, the load-displacement graphs displayed by (Peixinho et al., 2003) exhibited greater disparity between experiment and simulation for the TRIP steel in comparison to the DP steel. To address this issue and thereby correctly evaluate the advantage of the TRIP assisted PHS technology, where the optimal microstructure is achieved after hot forming and with retained austenite and hence mechanical properties more uniformly

distributed in the formed part, we propose a new modelling technique which more accurately simulates deformation of hot versus cold formed parts.

(Pavlina and Van Tyne, 2008) established a relationship between Vickers hardness (Hv) and yield strength (YS) by investigating over 150 hypoeutectoid steels having a wide range of chemical compositions and a variety of microstructures, including complex multiphase steels composed of bainite, martensite and retained austenite. The relationship is expressed by Equation 1.

$$YS = -90.7 + 2.876Hv \quad \text{(Eq. 1)}$$

(Pavlina and Van Tyne, 2008) acknowledge that while the relationship of Equation 1 is in very good agreement with experiment for ferritic and especially martensitic steels, the relationship is not so good for complex multiphase steels containing retained austenite. Thus, we add a correction factor of -166, giving rise to Equation 2. The correction factor was established by comparing predicted yield strength by Equation 1 to experimentally determined yield strength of the optimally press hardened 20MnSiAlPB5. Since we are concerned with just one chemical composition and just one heat treatment giving rise to just one microstructure, the simple correction factor can be considered valid for this investigation exclusively.

$YS = -90.7 + 2.876Hv - 166$ (Eq. 2)

The Vickers hardness measurements recorded at 0.5 mm intervals along the cross-section centreline of both hot and cold formed U-bend open box parts were converted to predicted yield strength with Equation 2, as illustrated by Fig. 19. Predicted yield strength was used to predict tensile engineering stress-engineering strain curves for each region (base, radius and side-wall) of the part geometry. For the hot formed part, predicted yield strength in each region of the part was similar (Fig. 19d), conforming closely to the experimentally determined value of the flat as-press hardened specimen. Thus, for the entirety of the hot formed part, the stress-strain curve of the flat as-press hardened specimen was considered to be representative. For the cold formed part, significantly higher hardness and thus predicted yield strength were found in the radius (Fig. 19c). Mean predicted yield strength in the radius was calculated as 725 MPa and used as the basis for the predicted stress-strain curve. Tensile testing was conducted on flat press hardened specimens pre-strained to 5 and 10 %, giving rise to yield strengths of 655 and 762 MPa respectively. Using these values as indicators, tensile testing was then conducted on flat press hardened specimens pre-strained to 8 %, giving rise to yield strength of 720 MPa and thus very close to the predicted yield strength of 725 MPa derived from Vickers hardness measurements. Pure bending theory (J.

Chakrabarty, 2006) states that given thickness of 1 mm and bending radius of 2 mm, maximum theoretical bending strain should be 20 %, as per Equation 3, where CD = length of outer edge (exposed to maximum tensile strain), AB = length of neutral axis (mm), R = radius of bend to neutral axis (mm), θ = angle of bend (radians) and y = distance from neutral axis AB to axis of interest CD (mm).

$$\varepsilon_{max} = \frac{\delta L}{L_o} = \frac{CD-AB}{AB} = \frac{(R+y)\times\theta - R\times\theta}{R\times\theta} = \frac{y}{R} = \frac{0.5}{2.5} = 0.2 \quad \text{(Eq. 3)}$$

The value of 20 % is somewhat higher than the experimentally estimated value of 8 %. However, note that in realty when stamping sheet metal into the corner of a die (without a blank holder), pure bending will not be present. Moreover, the value of 20 % represents the maximum theoretical strain, whereas the experimentally estimated value of 8 % represents the mean strain across the entire length and width of the radius. The stress-strain curve resulting from pre-strain to 8 % was thus considered to be representative of the radius of the cold formed part, with the base and side-wall represented by the stress-strain curve of the flat as-press hardened specimen without pre-strain. Fig. 7a presents representative engineering stress-engineering strain curves.

Engineering stress-engineering strain data were converted to true stress-true plastic strain. Since the true stress-true plastic strain data resulting from the conversion process are valid only

during uniform elongation to the commencement of necking, data were extrapolated over the full plastic strain range. This was conducted with Equation 4, as used by (Taylor et al., 2016), where σ = stress (MPa), σ_u = stress at necking (MPa), k = work hardening rate (MPa), ε = strain, ε_g = strain at necking and n = work hardening exponent. Fig. 7b presents the extrapolated true stress-true plastic strain curves.

$$\sigma = 0.5\left\{\left[\sigma_u + k(\varepsilon - \varepsilon_g)\right] + \left[\sigma_u \left(\frac{\varepsilon}{\varepsilon_g}\right)^n\right]\right\} \quad \text{(Eq. 4)}$$

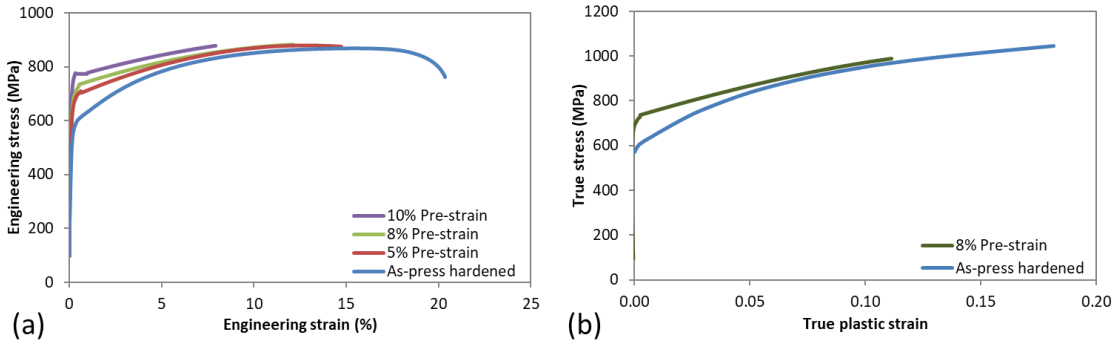

Fig. 7: Stress-strain curves used for numerical simulation (a) representative engineering stress-engineering strain (b) extrapolated true stress-true plastic strain

Transversal and axial crush testing were numerically simulated using the material data of Fig. 7b and the same part geometry and testing conditions of the physical experiments. This was performed in Abaqus CAE commercial software with a Dynamic Explicit model. Mesh size was 0.5 mm. Element type was Explicit 3D Stress. The isotropic hardening function incorporated in

Abaqus CAE was applied. Ductile damage was omitted for simplicity. Elastic modulus was entered as 210 GPa with Poisson's ratio of 0.3 and density of 7800 kg/m^3. For axial crushing, contact between the plates (modelled as Analytical Rigids) and box was modelled with a General Contact function carrying a friction coefficient penalty of 0.7. For transversal crushing, contact between the supports / former (modelled as Rigid Bodies) and box was modelled with a General Contact function carrying a friction coefficient penalty of 0.2. The different friction coefficients represent the different nature of contact and geometry; and are recommended for simulations of this kind. Simulation results are shown in the last section of `Results & Discussion`.

Results & Discussion

Press Hardening with Flat Dies for Tensile Testing and Optimisation of Process Parameters

Fig. 8 presents representative time-temperature plots from the start of cooling. Upon interrupting die-quenching and opening the tool, temperature increased due to substantial residual heat accumulation in the dies characterised by low thermal conductivity, before slow cooling commenced by natural air circulation. Even with the lowest tool-open temperature of 350 ^{o}C and longest tool-open time of 300 s, minimum temperature did not drop below 255 ^{o}C during the tool-open time, demonstrating capability of the new press hardening process to maintain substantial heat for the anisothermal bainitic ferrite transformation and carbon partitioning, without use of

secondary heating. Further, it is worth highlighting that in this lab scale experiment, the dies were relatively small, much smaller than dies found on industrial press hardening lines. Such industrial dies would exhibit much greater heat capacity for further retarded cooling. In such a case, water cooling of the dies could be regulated as necessary in order to achieve the exact conditions obtained from this lab scale experiment. Fig. 9 presents tool-open start temperature against mean tool-open temperature. With increased tool-open time, mean tool-open temperature decreased due to longer exposure to natural air cooling. As tool-open start temperature increased, or as soaking temperature increased, mean tool-open temperature increased due to greater residual heat accumulation at the moment of interrupted die-quenching. Even with the lowest soaking temperature of 950 ^{o}C, lowest tool-open temperature of 350 ^{o}C and longest tool-open time of 300 s, mean tool-open temperature was 375 ^{o}C, again demonstrating capability of the new press hardening process to maintain substantial heat for the anisothermal bainitic ferrite transformation and carbon partitioning, without use of secondary heating.

Fig. 10 presents tensile properties of press hardened 20MnSiAlPB5 (error bars have been omitted for clarity, while standard deviations are presented in Table 3). Proof strength (Rp0.2) increases with higher soaking temperature, presumably as the bainitic ferrite volume fraction decreases and the martensite volume fraction increases as a result of greater austenitic grain growth and hardenability. Proof strength decreases with longer tool-open time, likely as a result of

increased carbon partitioning from bainitic ferrite to austenite, which reduces interstitial solid solution strengthening of bainitic ferrite, which as the softest microconstituent, dictates proof strength. Proof strength decreases with increased tool-open temperature, which indicates a transition from martensite to lower bainite and then to upper bainite. The same observations can be made for ultimate tensile strength (Rm). Uniform elongation (Ag) is evaluated rather than total elongation (A5) in this instance since the uniform elongation value can be used as a strong indicator of a stress induced transformation enhancing ductility and is less susceptible to error than total elongation due to premature fracture of the test piece or fracture occurring outside the gauge length. Maximum uniform elongation was provided by soaking temperature of 950 ^{o}C. This is potentially due to a lower martensite volume fraction and finer bainitic ferrite grain size to enhance carbon partitioning rate and in turn, the stress induced transformation. Uniform elongation increases with soaking temperature raised from 1050 to 1150 ^{o}C. This is probably due to a coarser final microstructure resulting from greater austenitic grain growth at the higher soaking temperature. Moreover, after these higher soaking temperatures, the stress induced transformation is not present or negligible due to insufficient carbon partitioning. Thus, ductility of the final microstructure is dominated by conventional microstructural characteristics, such as grain size, rather than stress induced transformation. Uniform elongation increases with longer tool-open time, presumably due to increased carbon partitioning from bainitic ferrite to austenite, which

reduces interstitial solid solution strengthening of bainitic ferrite and enhances the stress induced transformation. Validation of the above is provided subsequently in discussion of microstructural analysis. The optimal parameters for 20MnSiAlPB5 can be highlighted as soaking temperature of 950 ^{o}C, tool-open temperature of 550 ^{o}C and tool-open time of 180 s, as presented in Table 2 along with the optimal parameters for 10MnSi15 and 20MnSi15. These parameters gave rise to the highest elongation values and the highest ultimate tensile strength-elongation product values (Rm*Ag and Rm*A5). The optimal tensile properties are summarised in Table 3. Fig. 11 presents ultimate tensile strength against proof strength (Fig. 11a) and ultimate tensile strength against total elongation (Fig. 11b) for the three steels press hardened to the full range of experimental parameters. The new press hardened steel 20MnSiAlPB5 failed to achieve the uniform elongation values of the two commercial steels (especially the lower carbon and softer 10MnSi15), which indicates a less effective stress induced transformation, but otherwise achieved similar properties to the commercial 20MnSi15, yet with a leaner and more manufacturer friendly chemical composition. The range of properties achievable from 20MnSiAlPB5 is also wider compared to the two commercial steels, indicating greater scope for a range of products. For example, soaking temperature of 1150 ^{o}C, tool-open temperature of 350 ^{o}C and tool-open time of 180 s gave rise to ultimate tensile strength of 1418 MPa and total elongation of 9.8 %. For the purpose of a ‘high strength product’, these values are far superior to those achieved from the two commercial steels

investigated and moreover, are comparable to results published in the literature, such as by (Liu et al., 2011) and (Xu et al., 2020) as discussed in the introduction section. It should be noted that (Liu et al., 2011) and (Xu et al., 2020) used marginally longer gauge lengths of 10 and 15 mm respectively (here we used 5 mm). Shorter gauge lengths have the effect of exaggerating the tensile elongation values. (Hanion et al., 2014) developed an equation for converting tensile elongation values between data obtained with different test-piece geometries. The reader is directed to the reference for further analysis and comparison between results. However, given the marginal difference in gauge lengths used here, by (Liu et al., 2011) and by (Xu et al., 2020), for all intents and purposes, the data presented are comparable. Moreover, it is again emphasised that here we achieve these properties with a leaner and more manufacturer friendly chemical composition; and with a more efficient press hardening process since modification to the press hardening line with a secondary heating step is not required.

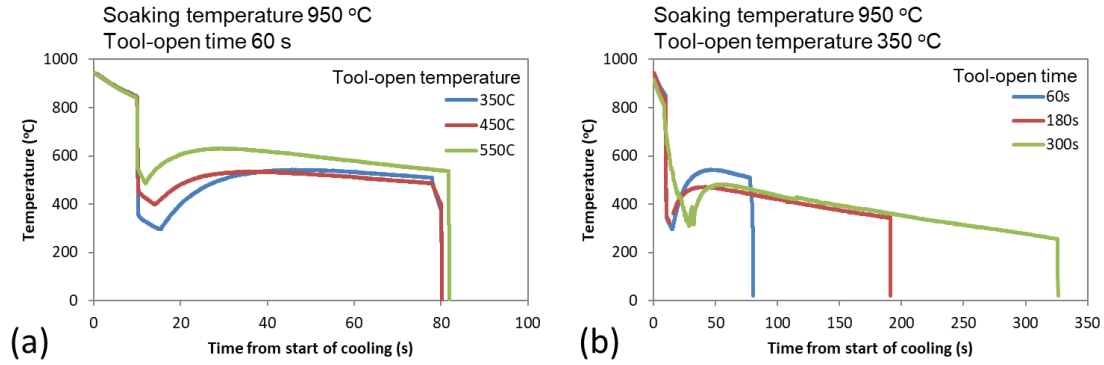

Fig. 8: Representative time-temperature plots (a) variable tool-open temperature (b) variable tool-open time

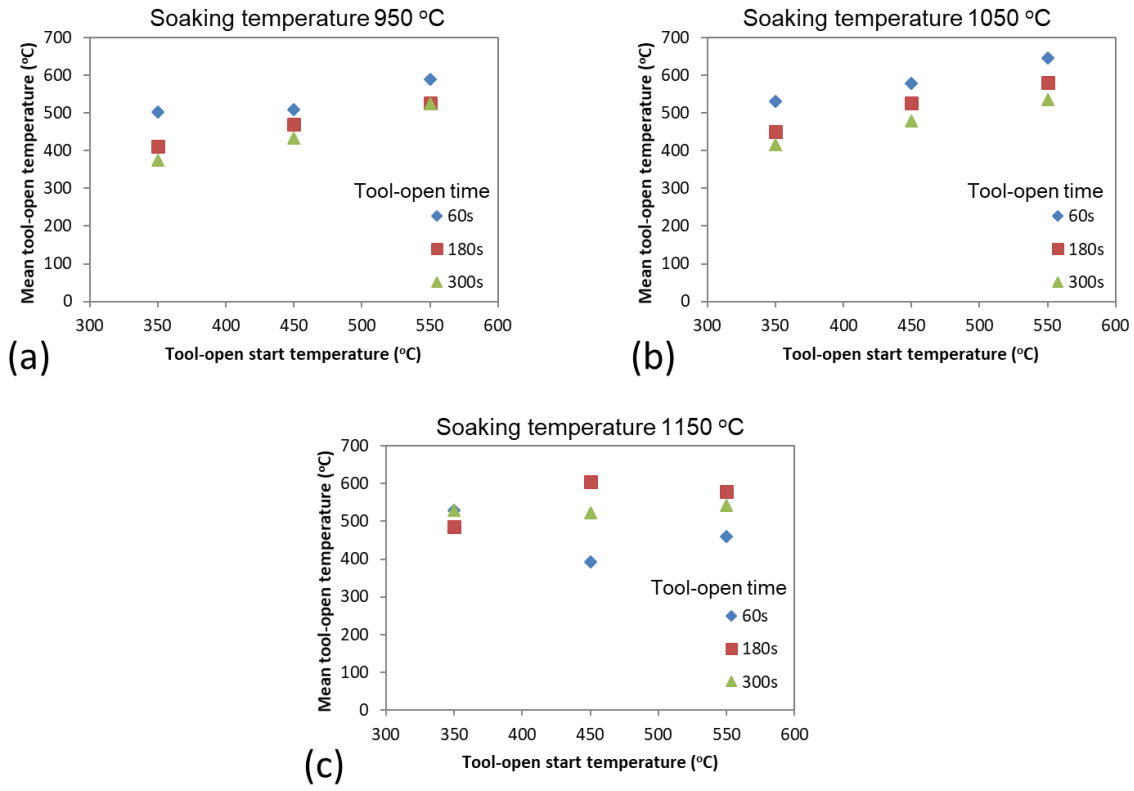

Fig 9: Tool-open start temperature against mean tool-open temperature

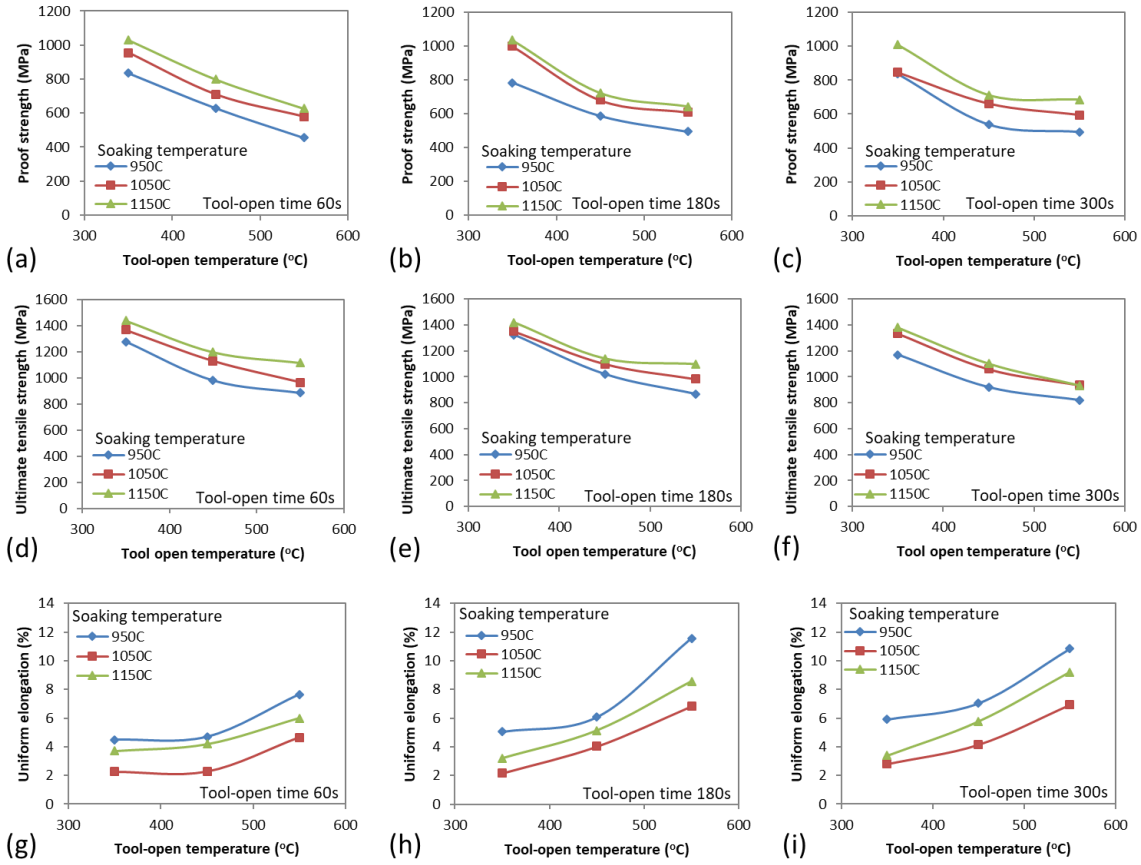

Fig. 10: Press hardened 20MnSiAlPB5 tensile properties

Table 2: Optimal press hardening parameters

	Soaking temperature (°C)	Tool-open temperature (°C)	Tool-open time (s)
20MnSiAlPB5	950	550	180
10MnSi15	950	450	300
20MnSi15	950	450	180

Table 3: Optimal tensile properties from press hardening

	Rp0.2 (MPa)	Rm (MPa)	Rp0.2/Rm	Ag (%)	A5 (%)	Rm*Ag (MPa.%)	Rm*A5 (MPa.%)
20MnSiAlPB5	495±71	867±62	0.57±0.02	11.6±3.1	20.5±4.1	9895±1721	17408±2043
10MnSi15	438±26	586±15	0.75±0.04	19.7±0.4	33.4±2.8	11510±375	19533±1242
20MnSi15	438±4	859±4	0.51±0.01	17.5±0.4	20.1±1.2	15025±426	17215±1103

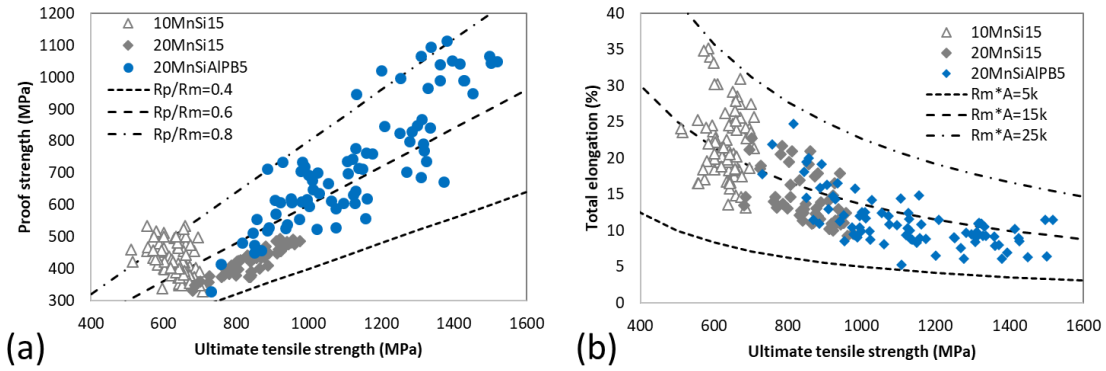

Fig. 11: Comparison between the new press hardened steel 20MnSiAlPB5 and the two commercial steels 10MnSi15 and 20MnSi15

Characterisation of Microstructure and the Stress Induced Transformation

Fig. 12 presents dilatometry plots for 20MnSiAlPB5 treated to the optimal press hardening parameters giving rise to the properties of Table 3. Note that absolute values of dilatometric strain

may be subject to error due to measurement by a modified thermo-mechanical testing machine rather than by a single-purpose dilatometer. However, trends depicted, namely contraction or expansion due to phase transformation, can be considered valid. To avoid variable thermal expansion rates from the heating rates used during press hardening and thus to clearly depict the ferrite to austenite transformation on heating, a continuous heating rate of 10 ^{o}C/s to 1200 ^{o}C was used (Fig. 12a). The ferrite to austenite transformation is completed by 938 ^{o}C, indicating that the new steel 20MnSiAlPB5 is completely austenitic at the soaking temperature of 950 ^{o}C and thus, can achieve complete austenisation with a soaking temperature typically used on industrial press hardening lines at present with MnB5 steels without requiring greater energy consumption. Progress of the ferrite to austenite transformation, estimated with the lever rule, is shown by Fig. 12b. On cooling (Fig. 12c), thermal contraction begins during the 10 s of transfer cooling time. As die-quenching begins, thermal contraction accelerates. Note that the rate of thermal contraction coincides with cooling rate. Also note that during dilatometry, die-quenching had to be simulated by forced air cooling, with the cooling rate achieved somewhat lower than that of die-quenching, yet sufficiently rapid to avoid the proeutectoid ferrite transformation. This highlights the novelty of the new TRIP assisted steel 20MnSiAlPB5 to provide sufficient hardenability under typical press hardening conditions. After approximately 30 s from the start of cooling, dilatation occurs, corresponding to the beginning of the tool-open time. Fig. 12d plots temperature against

dilatometric strain on cooling, from which dilatation and the corresponding phase transformation can be seen at the tool-open temperature of 550 °C. These observations firmly indicate that hot forming can take place in the exclusive austenite phase (for maximum formability) and that proeutectoid ferrite formation is avoided, with the transformation at 550 °C correlating with the predicated bainitic ferrite transformation of Fig. 4. Consequently, α-phase detected by EBSD and accounting for the majority of the microstructure at 48.3 % is clearly bainitic ferrite and not proeutectoid ferrite, as illustrated by representative phase distribution maps of Fig. 13. Further, the average misorientation angle is 37 °. The bainitic ferrite has an average grain size (diameter) of 2.7 (±1.8) μm. Despite continuous cooling during the tool-open time, dilatation continues (Fig. 12c), indicating continuous progression of the bainitic ferrite transformation and possible transition to the martensite transformation, given that after bainitic ferrite, the remainder of the microstructure consists of α'-phase (martensite) at 42.6 % and γ-phase (austenite) at 9.1 %. The martensite has an average grain size (corresponding to packet size) of 1.7 (±1.6) μm and average misorientation angle of 79 °, distinguishing it from bainitic ferrite. Given the low temperature, displacive and non-equilibrium nature of the martensite transformation, the misorientation angle of martensite can be expected to be significantly higher than that of other phases. The misorientation angle of martensite is often found to be above 50 ° (Gyhlesten Back and Engberg, 2017) and thus significantly higher than that of bainitic ferrite, which is often found to be less than 40 ° (Tu et al.,

2008). For comparison, phase distribution maps are also provided for 10MnSi15 and 20MnSi15 treated to their optimal press hardening parameters (Table 2) giving rise to the properties of Table 3. Since the three steels have been treated to different press hardening parameters, the microstructures are not directly comparable. Nonetheless, due to significantly different carbon content, the microstructure of 10MnSi15 is distinctly different from that of 20MnSiAlPB5 and 20MnSi15. The microstructure of 20MnSiAlPB5 is noticeably finer than the relatively blocky microstructure of 20MnSi15 and the retained austenite volume fraction is more than double. This illustrates the superiority of the new steel 20MnSiAlPB5 when used in combination with the new press hardening process.

The austenite volume fraction of 9.1 % measured by EBSD was confirmed by XRD, which recorded a comparable value of 11.7 %. Fig. 14a presents a representative XRD diffractogram, illustrating the austenite peak. The austenite volume fraction is indicative of carbon partitioning from bainitic ferrite during the tool-open time, since such a high volume fraction of retained austenite would not be expected otherwise. The austenite is ultra-fine, distributed between the bainitic ferrite and martensite boundaries with a small block or thin film morphology and with an average grain size (diameter) of 0.3 (±0.2) μm. With increasing tensile strain to 5 and then 10 %, the bainitic ferrite volume fraction remains relatively constant, while the austenite volume fraction deceases and the martensite volume fraction increases, as illustrated by Fig. 14b. This is

indicative of a stress induced transformation. With increasing tensile strain from 10 to 15 %, volume fractions remain relatively constant. This correlates with the uniform elongation value of 11.6 % (Table 3), since a stress induced transformation would be expected to be completed once strain has reached the uniform elongation value. Again, austenite volume fractions were confirmed by XRD, with similar values presented between EBSD and XRD. The austenite peak of the diffractogram becomes progressively more broad and less defined with increasing tensile strain applied to the specimen (Fig. 14a). This indicates lower reliability of the result and can be attributed to increasing distortion of the crystal lattice creating greater difficulty for the X-ray diffraction pattern to be correlated to the reference parameters. EBSD was thus the preferred characterisation tool for subsequent analyses. Nonetheless, the findings from EBSD and XRD demonstrate that the new steel 20MnSiAlPB5 achieves the objective of delivering a microstructure predominantly of bainitic ferrite, with dispersions of martensite and retained austenite; and with retained austenite undergoing a stress induced transformation to martensite during application of the formed part such as an automobile crash event, giving rise to the characteristically impressive strength-ductility combination of TRIP assisted steels. Moreover, by referring back to Table 3 and comparison to the two commercial steels, the new steel 20MnSiAlPB5, while relatively lean and manufacturer friendly, provides the optimal microstructural evolution observed within the constraints of the new press hardening process. For example, avoidance of proeutectoid ferrite

can be attributed to the novel boron addition to TRIP assisted steels, while the appreciable volume fraction of retained austenite and subsequent stress induced transformation despite limited time in the bainitic phase field under slow air cooling in the hot forming tool can be attributed to the novel Al, Si, P and Nb additions to PHS accelerating the bainitic ferrite transformation and carbon partitioning. Fig. 15 presents representative Inverse Pole Figure (IPF) crystallographic orientation maps. Following press hardening, the microstructure is relatively isotropic, both in terms of grain structure and texture intensity, with a relatively weak maximum texture intensity factor of just 1.9 (where texture intensity factor can be interpreted as the proportion of the microstructure that is orientated with the given crystallographic plane and direction combination). Since the final microstructure is relatively isotropic, we can infer that during hot forming, the microstructure was also isotropic. Isotropicity during hot forming is important for obtaining maximum formability. With increasing tensile strain following press hardening, the grain structure becomes progressively more deformed and the (111)[001] texture gradually develops, indicated by a maximum texture intensity factor of 4.3 after 15 % tensile strain.

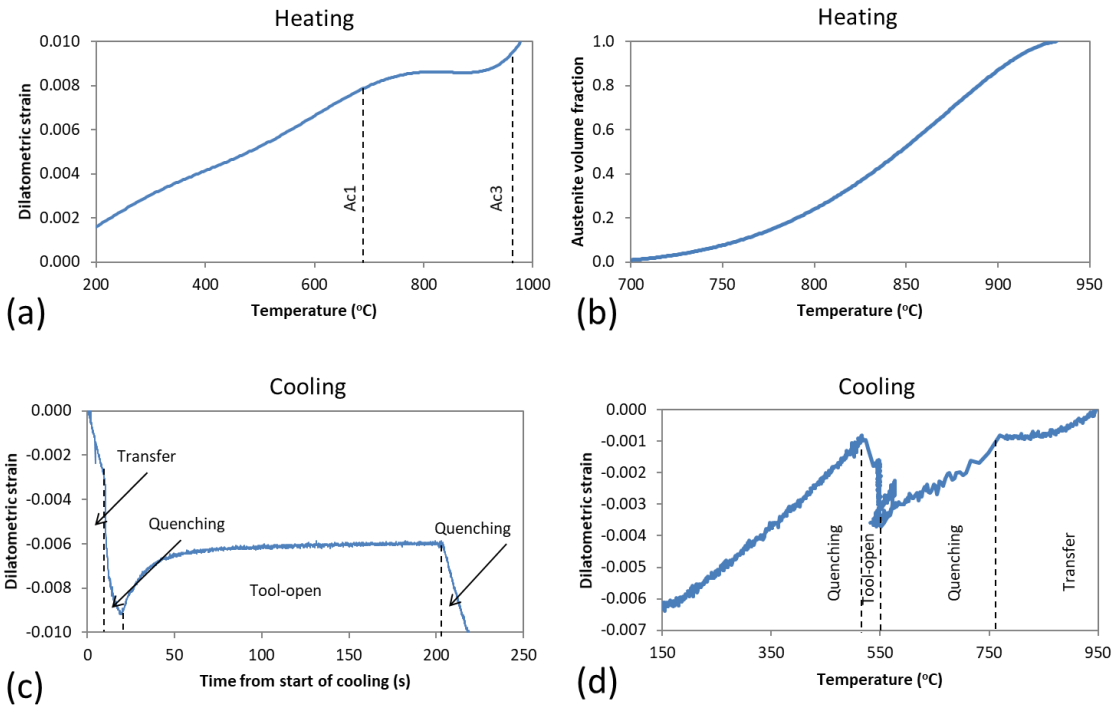

Fig. 12: 20MnSiAlPB5 dilatometry plots

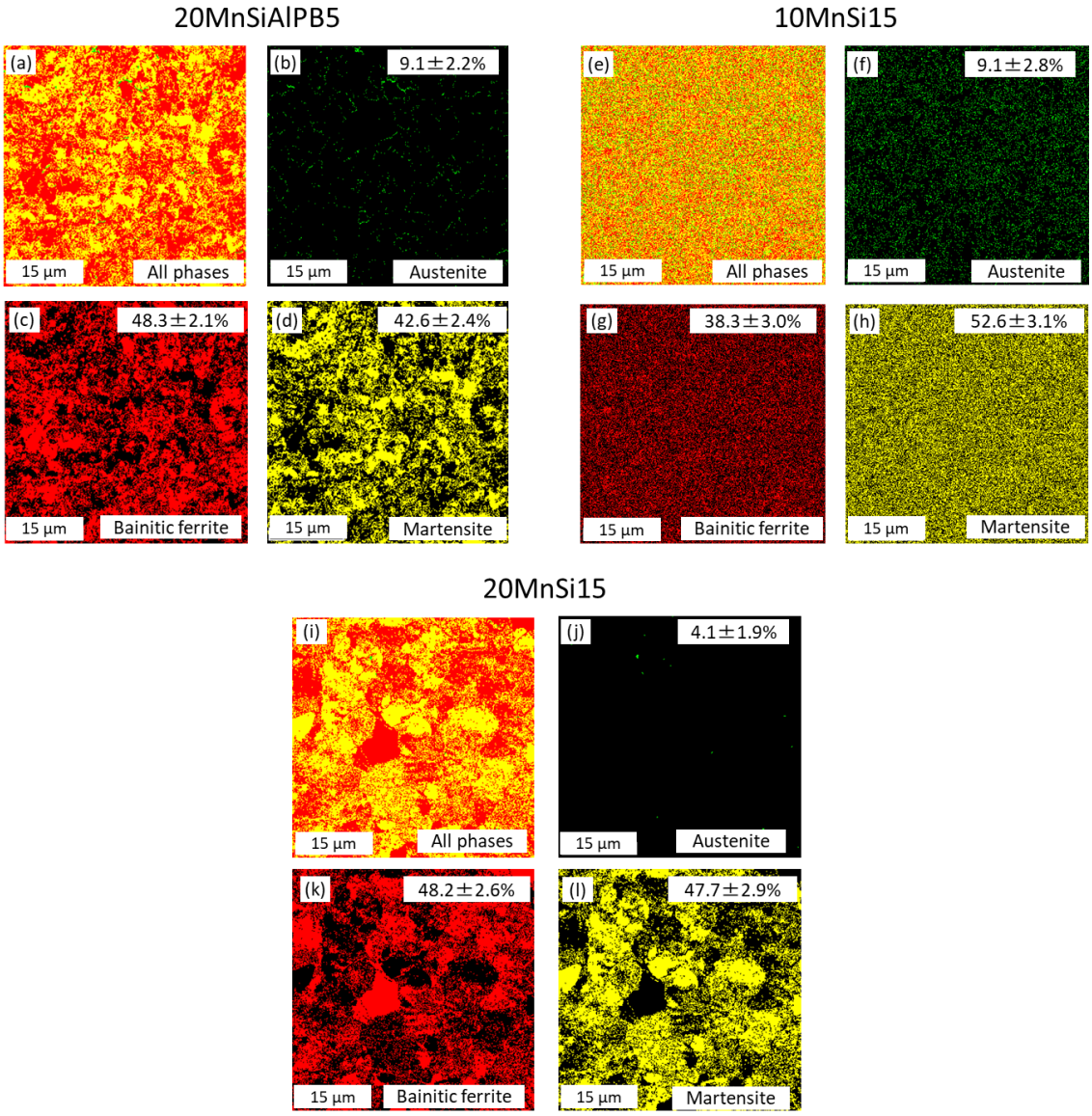

Fig. 13: EBSD phase distribution maps of press hardened 20MnSiAlPB5 (a-d), 10MnSi15 (e-h) and 20MnSi15 (i-l)

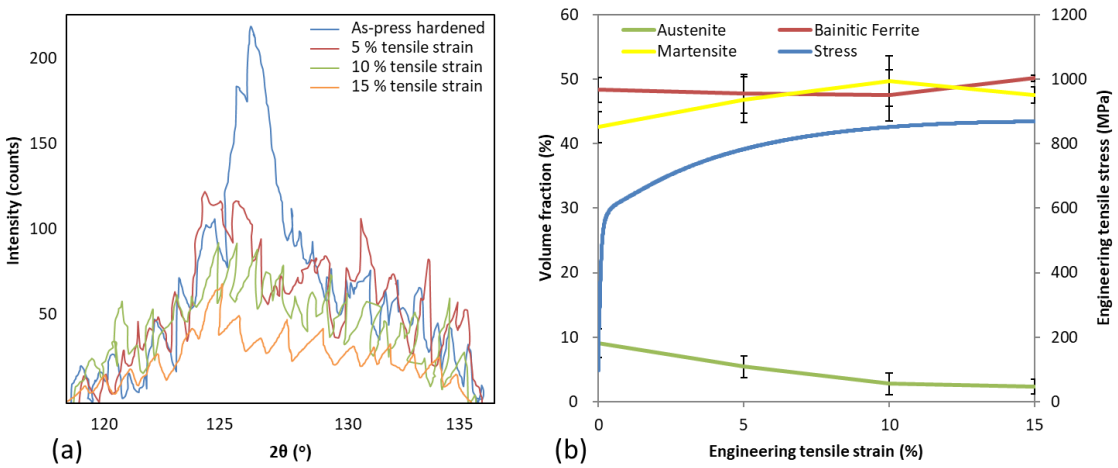

Fig. 14: Microstructural evolution with increasing tensile strain applied to press hardened 20MnSiAlPB5 illustrating the stress induced transformation (a) XRD diffractograms in the austenite range (b) volume fractions obtained from EBSD plotted against the stress-strain curve

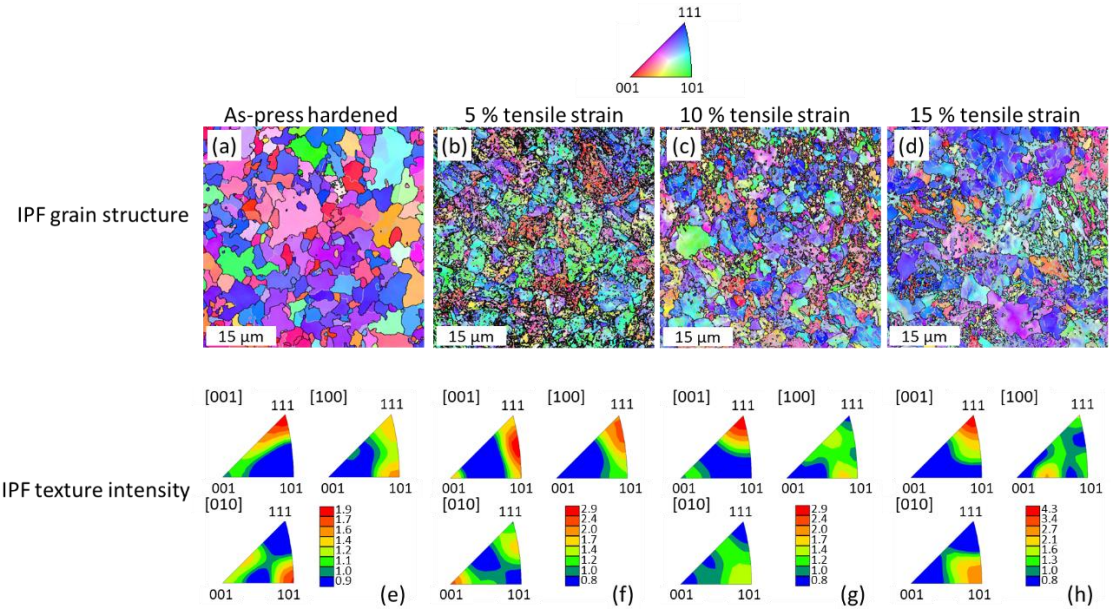

Fig. 15: EBSD crystallographic orientation maps of press hardened 20MnSiAlPB5 subjected to tensile strain

Transversal and Axial Crush Testing of Formed Parts

Fig. 16a illustrates representative load-displacement graphs from transversal crush testing. Curves have been corrected for slack take up by the testing machine during approximately the first 1.5 mm of displacement. Thus, maximum displacement is recorded as approximately 8.5 mm rather than the 10 mm applied. Note the two parts are composed of the same 20MnSiAlPB5 chemical composition and have been exposed to the same heat treatment (the optimal press hardening parameters), with the only difference being that one part has been cold formed (representative of traditional cold forming a TRIP assisted steel) and the other part has been hot formed according to the new press hardening process. The cold formed part exhibits higher stiffness (E), yield load (P_{yield}) and energy absorption (EA), but work hardening rate between 6-8 mm of displacement ($k_{6\text{-}8}$) of the hot formed part is significantly higher so that maximum load (P_{max}) of the two parts approach a near equivalent value, as summarised in Table 4. Fig. 16b illustrates representative load-displacement graphs from axial crush testing. Again, curves have been corrected for slack take up by the testing machine during approximately the first 2 mm of displacement. The cold formed part exhibits higher stiffness (E), but maximum load (P_{max}) is similar, while mean load (P_{mean}) and energy absorption (EA) of the hot formed part are higher, as summarised in Table 5. Fig. 16c illustrates representative energy absorbed-displacement graphs

from axial crush testing, from which the higher energy absorption of the hot formed part beyond approximately 5 mm of displacement, corresponding to conclusion of the first peak of the load-displacement graph, can be clearly observed. Moreover, the relatively smooth and consistent accumulation of energy absorption of the hot formed part, versus the relatively sporadic and non-predictable character of the cold formed part can also be observed. Fig. 16d presents images of parts following testing. While the cold and hot formed parts exhibit a similar appearance following transversal loading, there is a notable difference following axial loading. The hot formed part exhibits a smoother, more consistent and densely folded structure without buckling in the lower section. These differences can be correlated to the load-displacement graphs (Fig. 16b), where for the hot formed part, the rise and fall of load constituting each peak of the graph is of a smoother character. Each peak correlates to each fold of the deformed structure. The smooth and consistent folding behaviour combined with the consistent load maintenance and energy absorption can be correlated to the more uniform microstructure of the hot formed part. This is illustrated by the representative EBSD phase distribution maps. To enhance accuracy, rather than individual phase detection, characterisation is simplified into γ-phase (FCC) and α-phase (BCC). For the cold formed part (Figs. 17a-c), the retained austenite volume fraction decreases from 8.7 % in the base and 9.5 % in the side-wall (non-formed regions), to 3.3 % in the radius (formed region). For the hot formed part, phase volume fractions are similar in the three regions of the part

(Figs. 17d-f). While the initial retained austenite volume fraction before cold forming could be assumed to be 7-11 % (Fig. 13), it distributes in a narrow range of 6.5–8.0 % for the hot formed part, but in a wider range of 3.3-9.5 % for the cold formed part. This indicates that the stress induced transformation of austenite to martensite has occurred in the radii during cold forming. Fig. 18 presents representative IPF crystallographic orientation maps. For the cold formed part, work hardening giving rise to significant deformation of the grain structure and development of the (111)[100] texture is apparent in the radius, with a maximum texture intensity factor of 3.8. In contrast, for the hot formed part, the microstructure in the radius retains similar isotropic character of the base and side-wall, both in terms of grain structure and texture, with a relatively weak maximum texture intensity factor of just 2.6. The stress induced transformation coupled with work hardening of the cold formed part gives rise to significantly higher hardness in the radius, as illustrated by the hardness distribution profile of Fig. 19a. More uniform phase volume fractions throughout the cross-section of the hot formed part, coupled with no work hardening, gives rise to more uniform hardness throughout the cross-section (Fig. 19b). Hardness actually decreases slightly in the radius. This can be attributed to dynamic recrystallisation during hot forming and a lower cooling rate in the radius due to less homogenous contact with the water cooled forming tool during die-quenching. The differences observed between the hot and cold formed parts can be correlated to the crush properties. During both transversal and axial loading, the radii of the part

geometry are critical areas, since the application of load causes the part to bulge at the radii, as illustrated by the annotations in Fig. 16d. The higher hardness in the radii of the cold formed part thus increases part stiffness and yield load. Once yield load has been surpassed, the higher retained austenite volume fraction and greater capacity for stress induced transformation then accelerates work hardening in the hot formed part, giving rise to the higher work hardening rate observed. Once work hardening and the stress induced transformation have been exhausted, the two parts (cold formed and hot formed) are essentially in the same state, hence the maximum load is approximately equivalent. For parts of the automobile safety cell designed to minimise displacement and deflection, the hot formed part is arguably inferior. However, for parts of the crumple zones, designed to deform in a predictable and controllable manner for maximum energy absorption, the hot formed part and hence the new TRIP assisted PHS technology is clearly superior. The more uniform distribution of retained austenite coupled with the maximised stress induced transformation and work hardening capacity maximise mean load and energy absorption, with a 22 % increase to the latter. Moreover, frequency of load peaks and load amplitude are reduced, which are associated with predictable and controllable dissipation of impact energy and crash safety.

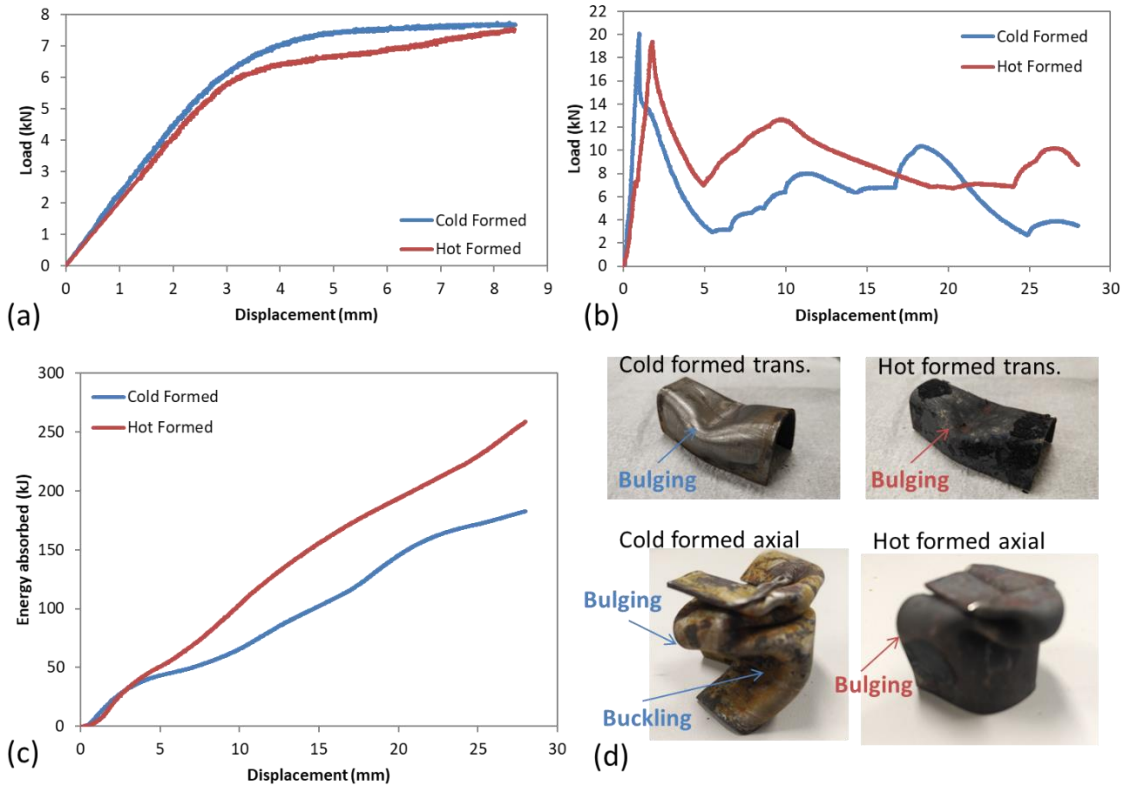

Figure 16: Crush testing (a) transversal load-displacement (b) axial load-displacement (c) axial energy absorbed-displacement (d) parts following crush testing

Table 4: Transversal crush test properties

	E (kN/mm)	P_{yield} (kN)	P_{max} (kN)	EA (kJ)	$k_{6\text{-}8}$ (kN/mm)
Cold Formed	2.2±0.3	5.6±0.9	7.7±1.3	50±7	0.07±0.01
Hot Formed	2.0±0.2	4.9±1.0	7.6±1.5	46±9	0.28±0.03

Table 5: Axial crush test properties

	E (kN/mm)	P_{max} (kN)	P_{mean} (kN)	EA (kJ)
Cold Formed	22.7±3.9	22.3±3.0	6.2±0.38	171±16
Hot Formed	14.0±5.1	21.3±2.7	9.1±0.15	241±25

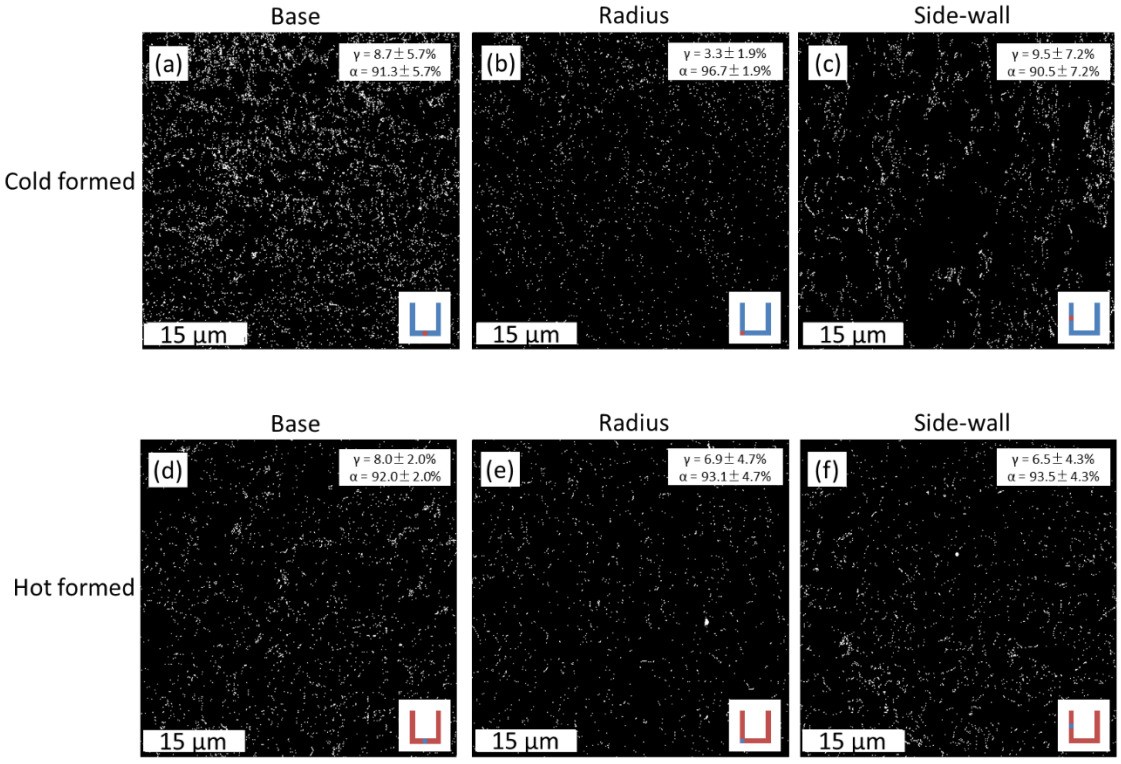

Fig. 17: Press hardened 20MnSiAlPB5 (a-c) EBSD phase distribution maps after cold forming (d-f) EBSD phase distribution maps after hot forming

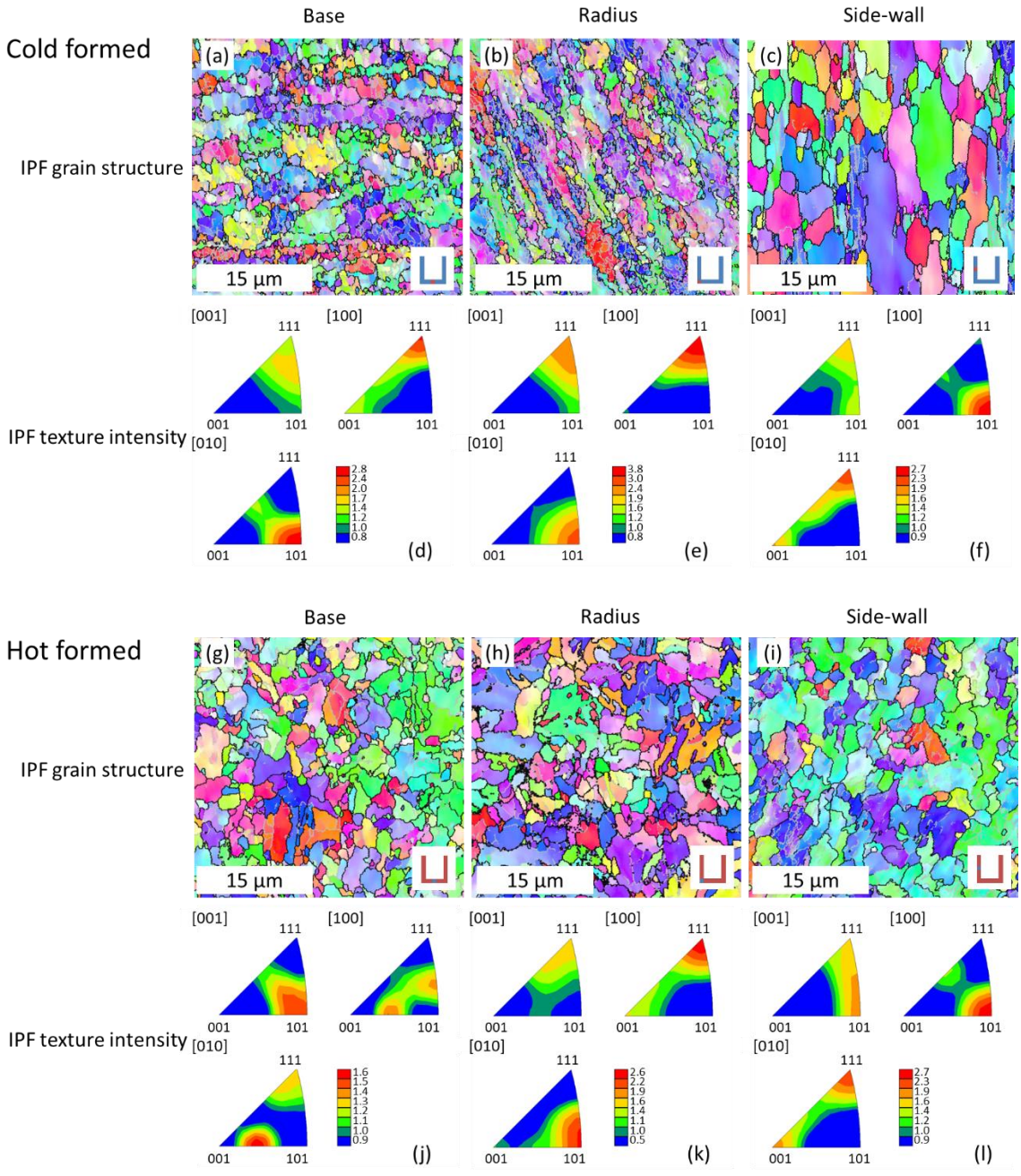

Fig. 18: EBSD crystallographic orientation maps of press hardened 20MnSiAlPB5 subjected to cold and hot forming (for IPF grain structure maps, the same legend key of Fig. 15 applies)

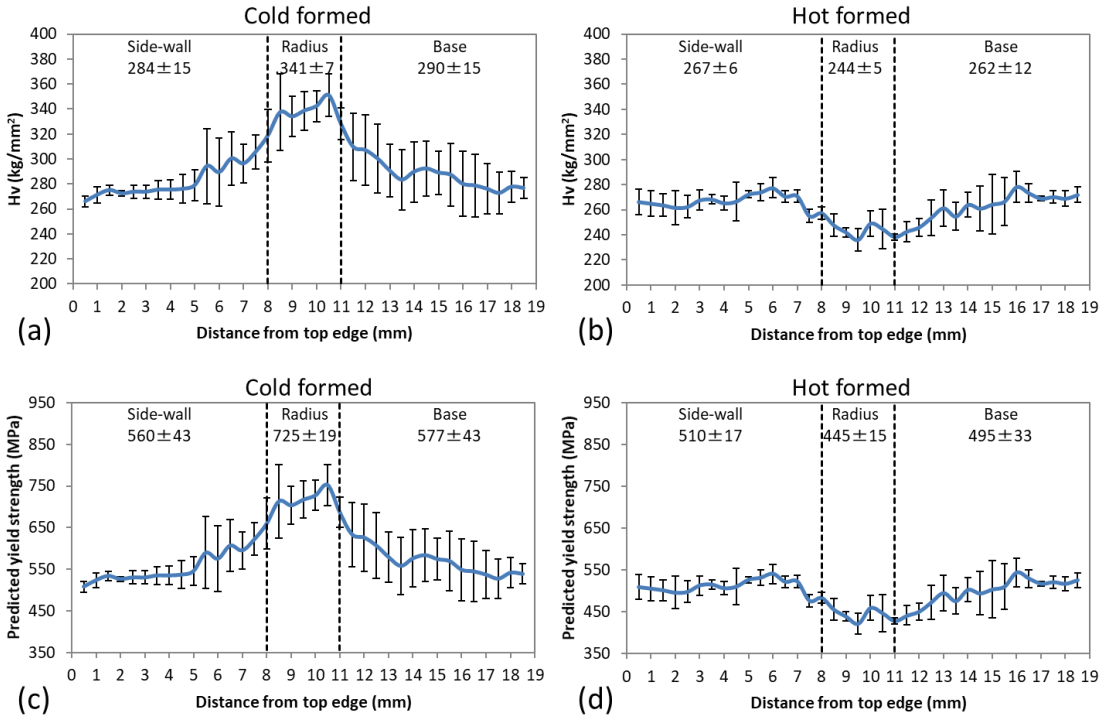

Fig. 19: Vickers hardness and predicted yield strength distribution profiles of press hardened 20MnSiAlPB5

Numerical Simulation of Transversal and Axial Crush Testing

Fig. 20a illustrates load-displacement graphs from numerical simulation of transversal crush testing, conducted with the material data of Fig. 7b. Curves have been truncated to 8.5 mm of displacement to be comparable to curves from the physical experiment. Compared to the physical experiment, the curves exhibit similar character, except for declining load (negative work hardening rate) beyond approximately 4 mm of displacement. The cold formed part exhibits higher stiffness and yield load, but the hot formed part exhibits marginally higher maximum load and

energy absorption, as summarised in Table 6. While the work hardening rate between 6-8 mm of displacement is negative, for the hot formed part, the value is closer to zero, thus following the same trend of the physical experiment. Differences between simulation and experiment can be attributed to inevitable inconsistencies in the experiment and imperfections in the material, whereas the simulation represents an idealised environment. Fig. 20b illustrates load-displacement graphs from numerical simulation of axial crush testing. Again, curves have been truncated to 28 mm of displacement to be comparable to curves from the physical experiment. Compared to the physical experiment, the curves exhibit similar character. The cold formed part exhibits higher stiffness and marginally higher maximum load, but mean load and energy absorption of the hot formed part are higher, as summarised in Table 7. These results are in very good agreement with the physical experiment and thereby, demonstrate that the new modelling technique, which accounts for the stress induced transformation and work hardening in the cold formed part, more accurately simulates deformation of hot versus cold formed parts. Fig. 20c illustrates energy absorbed-displacement graphs from numerical simulation of axial crush testing, from which the higher energy absorption of the hot formed part can be clearly observed. Fig. 20d presents von Mises stress colour contour maps of parts following loading. Following transversal loading, there is no notable difference between the cold formed part and hot formed part. Following axial loading, the hot formed part exhibits a smoother, more consistent and densely

folded structure without buckling of the lower section. The different appearance of the simulated parts closely replicates the physical experiment. Moreover, during both transversal and axial loading, accumulation of maximum stress in the radii of the part geometry, resulting from bulging at the radii, is clearly visible. This vividly demonstrates the importance of the radii to the formed part and thus, the merit of the new TRIP assisted PHS technology, where microstructure and mechanical properties are more uniform throughout the part cross-section, resulting in superior crash performance.

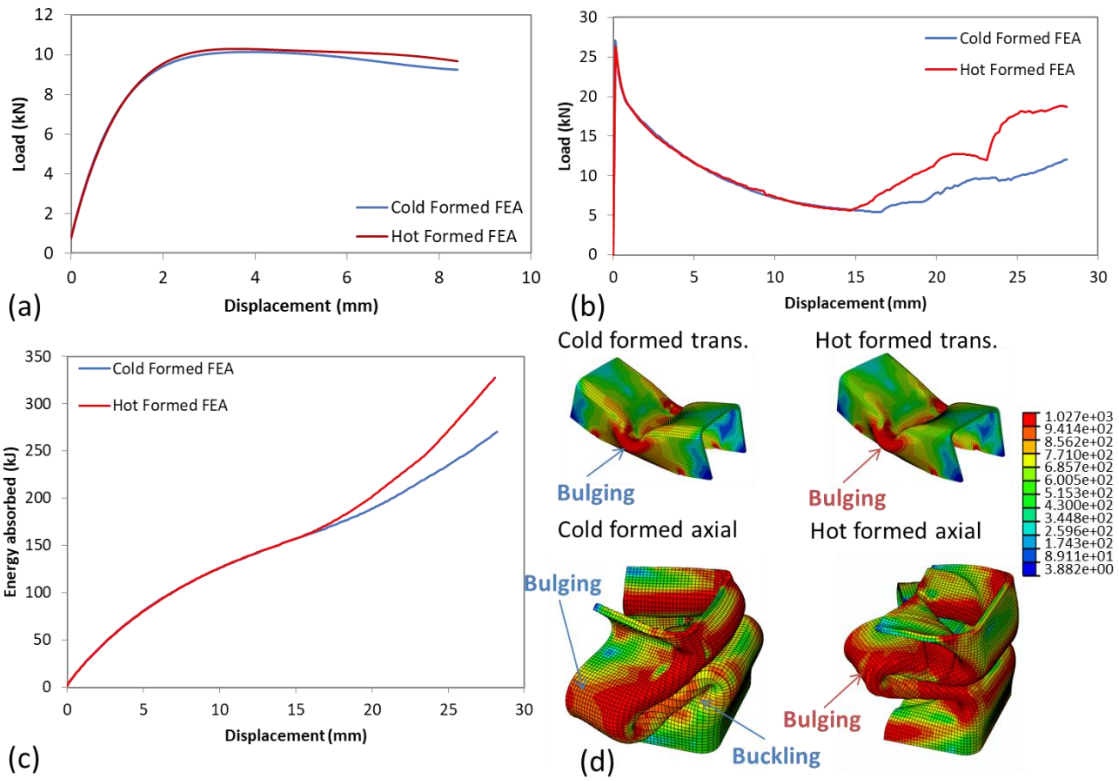

Figure 20: Numerical simulation of crush testing (a) transversal load-displacement (b) axial load-displacement (c) axial energy absorbed-displacement (d) parts following crush testing with von Mises stress colour contour maps

Table 6: Transversal crush test properties from numerical simulation

	E (kN/mm)	P_{yield} (kN)	P_{max} (kN)	EA (kJ)	$k_{6\text{-}8}$ (kN/mm)
Cold Formed	8.2	6.0	10.2	77	-0.28
Hot Formed	7.9	5.2	10.3	79	-0.16

Table 7: Axial crush test properties from numerical simulation

	E (kN/mm)	P_{max} (kN)	P_{mean} (kN)	EA (kJ)
Cold Formed	180.7	26.3	9.5	268
Hot Formed	175.6	26.1	11.6	328

Conclusion

- The optimised press hardened microstructure of 20MnSiAlPB5 consisted of 48.3 % bainitic ferrite, 42.6 % martensite and 9.1 % retained austenite.

- The retained austenite can undergo stress induced transformation to martensite during application of a formed part such as an automobile crash event, giving rise to 867 MPa tensile strength and 20.5 % total elongation.
- Traditional cold forming of TRIP assisted steel reduced the retained austenite volume fraction from 9.1 to 3.3 % in the formed radii, whereas the new TRIP assisted PHS technology more uniformly distributed the retained austenite in the formed part with a near equivalent volume fraction of 9.1 % throughout the part.
- The higher and more uniformly distributed retained austenite volume fraction enhanced energy absorption by 22 % during axial crushing.
- Numerical simulation of crush testing, including a new modelling technique which more accurately simulates deformation of hot versus cold formed parts, demonstrated accumulation of maximum stress in the formed radii and thus demonstrated the merit of the new TRIP assisted PHS technology.

Acknowledgments

This research was funded by the Japan Society for the Promotion of Science (JSPS).

References

V.F. Zackay, E.R. Parker, D. Fahr, R. Busch: The enhancement of ductility in high-strength steels, Transactions of the American Society for Metals, 60, 252-259, 1967

Y. Sakuma, A. Itami, O. Kawano, N. Kimura, S. Hiwatashi, K. Sakata: Next generation high-strength sheet steel utilising transformation-induced plasticity (TRIP) effect, Nippon Steel technical report, 64, 21, 1995

X. Tan, H. He, W. Lu, L. Yang, B. Tang, J. Yan, Y. Xu, D. Wu: Effect of matrix structures on TRIP effect and mechanical properties of low-C low-Si Al-added hot-rolled TRIP steels, Materials Science and Engineering: A, 771, 13, 2020

H.K.D.H. Bhadeshia: TRIP-Assisted Steels?, ISIJ International, 42, 9, 1059-1060, 2002

S. Oliver, G. Fourlaris, T.B. Jones: Dual Phase versus TRIP strip steels: a comparison of dynamic properties for automotive crash performance, Materials Science and Technology, 23, 4, 423-431, 2007

A. Mein, G. Fourlaris, D. Crowther, P.J. Evans: The influence of aluminium on the ferrite formation and microstructural development in hot rolled dual-phase steel, Materials Characterization, 64, 69-78, 2012

A. Bachmaier, K. Hausmann, D. Krizan, A. Pichler: Development of TBF steels with 980 MPa tensile strength for automotive applications: microstructure and mechanical properties, New Developments in Advanced High-Strength Sheet Steels, AIST, Vail, USA, 23-26 June 2013, 131-139, 2013

C.E. Ridderstrale, Norrbottens Järnverk AB: Manufacturing a hardened steel article, UK Patent GB 1490535-A, Sweden, filed 1974, published 1977

M. Naderi, M. Ketabchi, M. Abbasi, W. Bleck: Analysis of microstructure and mechanical properties of different boron and non-boron alloyed steels after being hot stamped, Procedia Engineering, 10, 460-465, 2011

H. Liu, X. Lu, X. Jin, H. Dong, J. Shi: Enhanced mechanical properties of a hot stamped advanced high-strength steel treated by quenching and partitioning process, Scripta Materialia, 64, 8, 749-752, 2011

Y. Xu, Y. Gong, H. Du, W. Ding, B. Zhu, X. Jin, Y. Zhang, L. Wang: A newly-designed hot stamping plus non-isothermal Q&P process to improve mechanical properties of commercial QP980 steel, International Journal of Lightweight Materials and Manufacture, 3, 1, 26-35, 2020

S. Oliver, T.B. Jones, G. Fourlaris: Dual phase versus TRIP strip steels: Microstructural changes as a consequence of quasi-static and dynamic tensile testing, Materials Characterization, 58, 4, 390-400, 2007

T. Taylor, D. Penney, J. Yanagimoto: One-step process for press hardened steel-carbon fibre reinforced thermoset polymer hybrid parts, Steel Research International, in-press（DOI: 10.1002/srin.202000085)

E.C. Bain: The alloying elements in steel, 1939, Pittsburgh, ASM International

N. Peixinho, N. Jones, A.C.M. Pinho: Experimental and numerical study in axial crushing of thin walled sections made of high-strength steels, Journal de Physique IV, 110, 717-722, 2003

E.J. Pavlina, C.J. Van Tyne: Correlation of yield strength and tensile strength with hardness for steels, Journal of Materials Engineering and Performance, 17, 888-893, 2008

J. Chakrabarty: Theory of Plasticity: 3rd Edition, Butterworth-Heinemann, 2006

T. Taylor, G. Fourlaris, J. Cafolla: Finite element modelling full vehicle side impact with ultrahigh strength hot stamped steels, Journal of Materials Engineering and Performance, 25, 10, 4495-4505, 2016

D.N. Hanlon, S.M.C. van Bohemen, S. Celotto: Critical assessment 10: tensile elongation of strong automotive steels as function of testpiece geometry, Materials Science and Technology, 31, 4, 385-388, 2015

J. Gyhlesten Back, G. Engberg: Investigation of parent austenite grains from martensite structure using EBSD in a wear resistant steel, Materials. 10, 5, article 453, 2017

M. Tu, W. Wang, Y. Hsu: Crystallographic and fractographic analysis of upper bainite, Materials Transactions, 49, 3, 559-564, 2008